

NAT'L INST. OF STAND & TECH R.I.C.
A11104 260254

NIST
PUBLICATIONS

NISTIR 5408

Characterization of the Hydrogen Induced Cold Cracking Susceptibility at Simulated Weld Zones in HSLA-100 Steel

**M. R. Stoudt
R. E. Ricker**

Corrosion Group

U.S. DEPARTMENT OF COMMERCE
Technology Administration
National Institute of Standards
and Technology
Materials Science and Engineering Laboratory
Metallurgy Division
Gaithersburg, MD 20899

Prepared for:

**Office of Naval Research
Department of the Navy
Arlington, VA 22217**

NIST

~~QC~~
100
.U56
1994
#5408

Characterization of the Hydrogen Induced Cold Cracking Susceptibility at Simulated Weld Zones in HSLA-100 Steel

**M. R. Stoudt
R. E. Ricker**

Corrosion Group

U.S. DEPARTMENT OF COMMERCE
Technology Administration
National Institute of Standards
and Technology
Materials Science and Engineering Laboratory
Metallurgy Division
Gaithersburg, MD 20899

April 1994

Prepared for:

**Office of Naval Research
Department of the Navy
Arlington, VA 22217**



**U.S. DEPARTMENT OF COMMERCE
Ronald H. Brown, Secretary**

**TECHNOLOGY ADMINISTRATION
Mary L. Good, Under Secretary for Technology**

**NATIONAL INSTITUTE OF STANDARDS
AND TECHNOLOGY
Arati Prabhakar, Director**

Characterization of the Hydrogen Induced Cold Cracking Susceptibility at Simulated Welds Zones in HSLA-100 Steel

**M. R. Stoudt
R. E. Ricker**

Abstract

The relative susceptibilities to hydrogen induced cold cracking were evaluated for HY-100, a steel presently in service in naval applications and for HSLA-100. The martensitic microstructure of the HY-100 undergoes wide variations in the heat affected zone during welding which strongly influence the resistance of that alloy to cold cracking. The HSLA-100, a low carbon, precipitation hardened steel with similar strength and toughness to that of the HY-100, possesses a significantly lower degree of hardenability which results in minimal microstructural variations in the heat affected zone under the same simulated welding conditions. The mechanical properties of the base metal and the heat affected zone created during a simulated, single welding pass were characterized by the slow strain rate technique for both steels in an inert environment and in artificial seawater under free corrosion and controlled hydrogen fugacities. The electrochemical behaviors of both steels were also evaluated in artificial seawater.

The results demonstrated that, in all cases, the performance of the HSLA-100 was equal or superior to that of the HY-100 over the range of hydrogen fugacities included in this evaluation and that the simulated weld heat affected zone of the HSLA-100 was generally less susceptible to hydrogen induced cold

cracking than the HY-100. Since the electrochemical behavior of the two alloys in artificial seawater was very similar, the observed differences in the susceptibilities to hydrogen cracking were attributed to the high degree of variability of the martensitic microstructure in the heat affected zone and to the influence of the size, shape and number of the inclusions present in the HY-100. At high hydrogen fugacity, the HSLA-100 demonstrated a good retention of ductility and the fracture surfaces showed less pronounced transgranular cleavage-like cracking, whereas the HY-100 exhibited a trend toward greater embrittlement with more significant transgranular cleavage-like fracture.

Table of Contents

| | |
|------------------------------|----|
| Abstract | i |
| List of Tables | iv |
| List of Figures | v |
| Introduction | 1 |
| Experimental | 12 |
| Results | 17 |
| Slow strain rate tests | 17 |
| Electrochemistry | 18 |
| Microstructure | 19 |
| Fractography | 20 |
| Discussion | 23 |
| Conclusions | 31 |
| Acknowledgement | 33 |
| References | 34 |

List of Tables

| | | Page |
|---------|--|------|
| Table 1 | Chemistries of the Two High Strength Steel Alloys. | 37 |
| Table 2 | Free Corrosion Potentials Measured in ASTM Artificial Seawater. | 38 |
| Table 3 | Mechanical Properties of the HY-100 Parent Metal. | 39 |
| Table 4 | Mechanical Properties of the HY-100 Simulated Heat Affected Zone. | 40 |
| Table 5 | Mechanical Properties of the HSLA-100 Parent Metal. . . | 41 |
| Table 6 | Mechanical Properties of HSLA-100 Heat Affected Zone. | 42 |
| Table 7 | Quantitative Metallography Data. | 43 |

List of Figures

| | Page |
|---|------|
| Figure 1 The relationship between the actual carbon content, the carbon equivalent and the susceptibility to hydrogen induced cracking. | 44 |
| Figure 2 The temperature-time command profile used to create the simulated heat affected zone resulting from a single welding pass. | 45 |
| Figure 3 A schematic diagram of the electrochemical cell used in the slow strain rate testing. | 46 |
| Figure 4a The ultimate tensile strength vs electrode potential for the HY-100 parent metal and heat affected zone in recirculating ASTM artificial seawater. | 47 |
| Figure 4b The ultimate tensile strength vs electrode potential for the HSLA-100 parent metal and heat affected zone in recirculating ASTM artificial seawater. | 47 |
| Figure 5a The strain to failure vs electrode potential for the HY-100 parent metal and heat affected zone in recirculating ASTM artificial seawater. | 48 |
| Figure 5b The strain to failure vs electrode potential for the HSLA-100 parent metal and simulated heat affected zone in recirculating ASTM seawater. | 48 |
| Figure 6a The reduction in area vs electrode potential for the HY-100 parent metal and heat affected zone in recirculating ASTM artificial seawater. | 49 |
| Figure 6b The reduction in area vs electrode potential for the HSLA-100 parent metal and heat affected zone in recirculating ASTM artificial seawater. | 49 |
| Figure 7a Potentiodynamic scan of the HY-100 parent metal and heat affected zone in aerated ASTM artificial seawater at 1mV/sec scan rate. | 50 |

| | | |
|------------|---|----|
| Figure 7b | Potentiodynamic scan of the HY-100 parent metal and heat affected zone in deaerated ASTM artificial seawater at 1mV/sec scan rate. | 50 |
| Figure 8a | Potentiodynamic scan of the HSLA-100 parent metal and heat affected zone in aerated ASTM artificial seawater at 1mV/sec scan rate. | 51 |
| Figure 8b | Potentiodynamic scan of the HSLA-100 parent metal and heat affected zone in deaerated ASTM artificial seawater at 1mV/sec scan rate. | 51 |
| Figure 9a | Comparison of the potentiodynamic scans for the HY-100 and the HSLA-100 parent metals in deaerated ASTM artificial seawater at 1mV/sec scan rate. | 52 |
| Figure 9b | Comparison of the potentiodynamic scans for the HY-100 and the HSLA-100 heat affected zones in deaerated ASTM artificial seawater at 1mV/sec scan rate. | 52 |
| Figure 10a | As polished view of the HY-100 parent metal showing the size and distribution of the observed inclusions. | 53 |
| Figure 10b | As polished view of the HSLA-100 parent metal showing the size and distribution of the observed inclusions. | 53 |
| Figure 11a | Optical micrograph of the HY-100 parent metal showing the quenched and tempered microstructure. (CLQ-1 etch) | 54 |
| Figure 11b | Optical micrograph of the HSLA-100 parent metal showing the bainitic structure and niobium carbonitride precipitates. (CLQ-1 etch) | 54 |
| Figure 12a | Optical micrograph of the HY-100 weld heat affected zone showing the greatest observed deviation from the parent metal microstructure. (CLQ-1 etch) | 55 |

| | | Page |
|------------|---|------|
| Figure 12b | Optical micrograph of the HSLA-100 weld heat affected zone showing the greatest observed deviation from the parent metal microstructure. (CLQ-1 etch) | 56 |
| Figure 13a | The variation in micro-hardness as measured from the center of the gauge section for the HY-100 heat affected zone. | 56 |
| Figure 13b | The variation in micro-hardness as measured from the center of the gauge section for the HSLA-100 heat affected zone. | 57 |
| Figure 14a | Low magnification scanning electron micrograph of the HY-100 heat affected zone showing the characteristic ductile behavior observed in the failures contained in Region I of Figure 6. | 57 |
| Figure 14b | High magnification scanning electron micrograph from Figure 14a showing the size and distribution of the observed microvoids. | 58 |
| Figure 15a | Low magnification scanning electron micrograph of the HSLA-100 heat affected zone showing the characteristic ductile behavior observed in the failures contained in Region I of Figure 6. | 58 |
| Figure 15b | High magnification scanning electron micrograph from Figure 15a showing the general size and distribution of the observed microvoids. | 59 |
| Figure 16a | Low magnification scanning electron micrograph of the HY-100 heat affected zone showing the embrittled behavior observed in failures contained in Region III of Figure 6. | 59 |
| Figure 16b | High magnification scanning electron micrograph from Figure 16a showing the nature of the transgranular cleavage-like cracking observed. | 59 |

| | | Page |
|------------|---|------|
| Figure 17a | Low magnification scanning electron micrograph of the HSLA-100 heat affected zone showing the embrittled behavior observed in failures contained in Region III of Figure 6. | 60 |
| Figure 17b | High magnification scanning electron micrograph from Figure 17a showing the nature of the transgranular cleavage-like cracking observed. | 60 |
| Figure 18 | Low magnification scanning electron micrograph of the HY-100 heat affected zone showing the mixed mode behavior observed in failures contained in Region II of Figure 6. | 61 |
| Figure 19 | Low magnification scanning electron micrograph of the HSLA-100 heat affected zone showing the mixed mode behavior observed in failures contained in Region II of Figure 6. | 61 |
| Figure 20a | Low magnification scanning electron micrograph of the HY-100 parent metal showing the embrittled behavior in failures contained in Region III of Figure 6. | 62 |
| Figure 20b | High magnification scanning electron micrograph from Figure 20a showing the nature of the transgranular cleavage-like cracking observed. | 62 |
| Figure 21a | Low magnification scanning electron micrograph of the HSLA-100 parent metal showing the embrittled behavior in failures contained in Region III of Figure 6. | 63 |
| Figure 21b | High magnification scanning electron micrograph from Figure 21a showing the nature of the transgranular cleavage-like cracking observed. | 63 |

INTRODUCTION

The continuing need for high performance materials for use in structural and military applications has led to the development of several classes of “ultra-service” alloy steels, specifically, the high yield stress series (HY) and the high strength low alloy steels (HSLA’s). Both of these alloy classes demonstrate excellent strength to weight ratios, fracture toughness and, in most cases, good corrosion resistance.^{1,2} In the early 1980’s, the US Navy certified HSLA-80, a low carbon, precipitation hardened steel with a nominal yield stress of 80 ksi (550 MPa), for use in ship construction. This alloy was equal to the HY-80, already in service, in strength and fracture toughness but was far superior to the HY-80 in weldability.^{2,3,4} Because it did not require post weld heat treatments, the use of the HSLA-80 alloy resulted significant cost reductions during the constructions of the Ticonderoga Class cruisers and the Nimitz Class aircraft carriers and, to further reduce fabrication costs, the Navy began development of HSLA-100 as a replacement for HY-100.³ Like HSLA-80, HSLA-100 is also a low carbon, precipitation hardened steel, equal to its HY counterpart in strength and fracture toughness and does not require a complicated welding procedure.^{3,4}

The HY-100 alloy was developed around the principle that high chromium and carbon contents (1.6 percent and 0.2 percent respectively) produce an effective degree of hardenability so that the desired strength and toughness levels can be achieved by appropriate quench and temper operations. In contrast, the composition of the HSLA-100 has very low carbon and chromium contents (0.02 percent and 0.6 percent respectively). The strength levels in this alloy are

achieved by precipitation of a fine epsilon-copper phase and niobium carbonitride particles.^{5,6,7} This produces a steel that exhibits exceptional fracture toughness (1.5 to 2 times higher than HY-100) with a low degree of hardenability which results in better welding properties.^{3,4}

A weld is composed of three distinct regions or zones: (1) the unaltered base or parent metal, (2) the fusion zone and (3) the heat affected zone (HAZ).^{8,9} In the HAZ, the microstructure, chemical composition and mechanical properties can vary dramatically with distance from the fusion boundary. The nature and extent of these variations have a strong influence on the resistance of the HAZ to post-weld cold cracking. Of course, the nature and extent of these variations depend on the composition of the steel and on the welding conditions—specifically, the heat input.¹⁰ The heat input into the weld determines the magnitude of the thermal gradient and the cooling rate which, coupled with the composition of the steel, determines the microstructure and the properties.^{8,9,10,11,12} Depending on the composition and hardenability of the steel, this may result in considerable variations in the mechanical properties through the weld zone.¹⁰

Microstructures with the same chemical composition can have very different susceptibilities to cold cracking.¹⁰ Twinned martensite is considered to be the most susceptible microstructure because of the high residual stresses contained within.^{13,14} Tempering greatly reduces the susceptibility of martensitic structures to cold cracking.^{10,15} Lower carbon lath martensite, bainitic structures, are much less susceptible to cold cracking and fully transformed ferrite-pearlite is the least susceptible microstructure.^{10,13,15,16}

Carbon is recognized as the alloying element with the greatest influence on the hardenability and cold cracking susceptibility of steels, but other alloying elements such as molybdenum and chromium also have strong influences on hardenability.^{2,10,17} While nickel also increases the hardenability of steels, it has been shown to reduce the cold cracking susceptibility¹⁰. Similar beneficial influences have been demonstrated by niobium and manganese.¹⁰

Graville demonstrated that the cold cracking susceptibility of steels can be classified according to the composition and hardenability of the steel.⁹ By plotting a slightly modified version of the standard relationship for the carbon equivalent against the actual carbon content of steels, Graville found three different regions of cold cracking behavior result as shown in Figure 1. In this figure, steels with compositions in Zone I contain very little carbon ($<0.1\%$), exhibit little hardenability, and for most welding conditions, exhibit very little cold cracking. Zone II steels contain significant amounts of carbon, but contain only small quantities of the alloying elements which increase hardenability. As a result, the microstructures, hardness, and the cold cracking resistance of the HAZ's formed in these steels vary greatly with the welding conditions. Zone III steels contain significant quantities of both carbon ($>0.1\%$) and alloying elements that increase hardenability. As a result, martensitic structures readily form during welding of these steels resulting in HAZ's which are susceptible to cold cracking. Therefore, welding of these steels require heat treatments and other special procedures which increase fabrication costs to avoid cold cracking.^{9,10} The HY-100 alloy, presently used for ship fabrication, is a Zone III steel.

Examination of Figure 1 indicates that significant quantities of alloying elements can be added to a low carbon steel without increasing the cold cracking susceptibility. That is, it should be possible to create a steel which is strengthened with the alloying elements used in the carbon equivalent equation without increasing the susceptibility of the steel to cold cracking. HSLA-100 is designed to be a high strength steel with a Zone 1 composition and good resistance to cold cracking at welds.

Cold cracks form at low temperatures (below 200°C) in either the weld metal or in the adjacent HAZ.⁹ These cracks most often initiate along the root of the fusion boundary at or near nonmetallic inclusions and may extend well into the base metal.¹⁰ Several investigators have found that cold cracking results when hydrogen is present in a weld zone with a susceptible microstructure and stress (either applied or residual).^{10,13,14,15,16,18} While the growth rate of these sub-critical cracks is usually very slow, these cracks may grow to critical size and cause failure.^{8,9,10}

The size, shape and distribution of the inclusions in a steel influence the deformation and fracture behavior of the steel. The stress concentrations associated with inclusions will be lower in steels with smaller and more spherical inclusions. As a result, a steel with smaller and more spherical inclusions will sustain more plastic deformation before nucleation of microvoids (dimples), transgranular cleavage, or other fracture modes.¹⁹

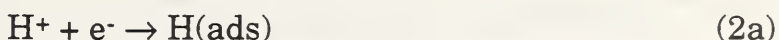
Hydrogen may enter the weld zone from many sources such as hydrogen gas molecules in the atmosphere, hydrogen in the welding consumables, or water present in the fluxes or on the metal surfaces during welding. Hydrogen may

also enter the weld zone as a result of corrosion in the service environment.^{17,18,20} The solubility of hydrogen in steel is very dependent on temperature and pressure, following Sievert's relationship:¹⁰

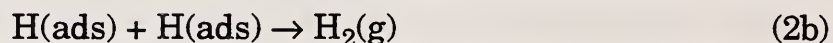
$$S=k[P]^{1/2} \quad (1)$$

Where S is the solubility of hydrogen, P the ambient pressure and k a constant dependent on temperature. The deleterious effects associated with absorbed hydrogen are independent of the hydrogen source, but they can be prevented by removing the hydrogen or by keeping the hydrogen content below some critical level. This can be accomplished by pre and post-welding heat treatments for both the steel being welded and the consumables used in the welding procedure.

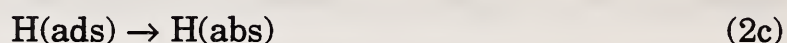
Exposure of a steel structure to the aggressive seawater environment present in most naval applications usually results in general corrosion of the metallic components. Cathodic protection, one of the more common methods used to protect these structures from the environment, utilizes a galvanic coupling with an active metal (such as zinc) to suppress the active corrosion reactions. However, the potential gradients resulting from the cathodic protection process may generate hydrogen which could then have an adverse effect on the steel. During corrosion, the reaction which removes the electrons generated from the ionization of atoms on the metal surface frequently evolves hydrogen according to the reaction:



The adsorbed hydrogen created by this reaction can be removed from the surface of the metal by either the formation of a gas bubble according to the recombination reaction:



or by absorption into the metal according to the reaction:



The equilibrium fugacity of hydrogen generated from equation (2a) and (2b) varies with potential and pH according to the Nernst equation:

$$E(V_{\text{NHE}}) = \frac{RT}{F} \ln \left\{ \frac{[\text{H}^+]}{[\text{H}_2]^{0.5}} \right\} \quad (3)$$

where $E(V_{\text{NHE}})$ is the potential measured with respect to a hydrogen electrode, R is the gas constant, F is the Faraday constant, T is the absolute temperature and the bracketed quantities are the activities. Assuming that the hydrogen in the steel is in equilibrium with the hydrogen adsorbed on the surface of the steel (equilibrium for equation (2c)), then the fugacity of the hydrogen absorbed in the steel will be equal to that given by equation (3). While this treatment assumes

equilibrium, it is common practice to use the hydrogen fugacity determined from this relationship as a reasonable estimate of the relative magnitude of the actual hydrogen fugacity and to assume that experiments conducted at the same potential with respect to the hydrogen electrode to be conducted at the same hydrogen fugacity. It should be kept in mind that under non-equilibrium conditions, such as hydrogen gas bubbling, the hydrogen fugacity calculated from equation (3) may vary greatly from the actual value due to local changes in pH, irreversible losses, and mass transport. However, for two alloys with essentially identical electrochemical properties, the actual fugacity will vary with potential in the same manner and control of the potential with respect to a reference electrode is a good means of measuring and controlling the relative hydrogen fugacity.

Absorbed hydrogen diffuses rapidly into pure iron where it generally remains as homogeneously distributed protons in solid solution at interstitial sites within the body centered cubic iron lattice. However, in a steel, hydrogen is not homogeneously distributed and frequently segregates to microstructural discontinuities such as inclusions and second phase interfaces.^{14,18,20} This effect is often referred to as hydrogen trapping.^{18,21} The concentration of hydrogen at these structural discontinuities, or trap zones, tends to be substantially higher than the bulk concentration. This is partially due to the high degree of hydrogen mobility within the iron lattice resulting from the disparity between the sizes of hydrogen and iron atoms. Also, the stress fields associated with dislocations and grain boundaries are known to provide lower energy sites for the hydrogen than the normal interstitial positions.^{17,18,20,22,23} This results in an increase in the apparent hydrogen solubility and a decrease in the apparent diffusivity in

materials containing high concentrations of microstructural imperfections.^{14,18,22,20} Also, the ability of these defects to trap hydrogen at their interfacial regions is known to depend on their number, size, and shape.^{24,25} Hydrogen is transported to these trapping regions by dislocation motion or by other diffusion processes. Due to its higher mobility, the dislocation core may transport hydrogen at a rate much higher than that of lattice diffusion, at the same temperature, and result in a higher degree of localization.^{17,24} In addition to being a transport mechanism, the cores of dislocations are known to act as effective hydrogen traps.^{18,20,22} It has been demonstrated that the number of available trapping sites in a steel markedly increases with plastic deformation, much like the way deformation increases the dislocation density, and since the migration of hydrogen to the trap region appears to be more energetically favorable, it would follow that the mobility of hydrogen in a steel should markedly decrease with deformation.¹⁸ While it is true that most of the absorbed hydrogen will be located in the region of the imperfections, a single trapping site has a finite hydrogen capacity. Some microstructural defects such as grain boundaries, precipitates and dislocation cores form a class of trap that only weakly binds to the hydrogen. These are often referred to as reversible, or temporary, trapping sites.^{16,18,21,24} These heterogeneously distributed, low binding energy (20-30 kJ/mole) traps are believed to play a very important role in the kinetics of hydrogen transport.²⁴ The result of this action is a more efficient means of rapid hydrogen transport either to traps with stronger binding energy (~100kJ/mole) or to regions of local failure, effectively enhancing embrittlement.^{21,23,24}

In general, low carbon steels with yield stresses below 500 MPa do not exhibit signs of hydrogen embrittlement, but as the levels of carbon are increased, the susceptibility to embrittlement also increases, due to the higher number of low energy sites that are filled by the carbon, thus limiting the overall ability to trap hydrogen.^{16,17,26,27} The influence of absorbed hydrogen on the behavior of high strength steels has been the subject of extensive research and several complex mechanisms describing the embrittlement process have been proposed.^{14,20,22,28,29,30} Among these are: 1) the planar pressure model, 2) the decohesion model and 3) the enhanced plasticity model. The planar pressure model is based on the hypothesis that absorbed hydrogen precipitates in molecular form at internal voids within the metal lattice.³¹ The pressure resulting in the bubble formed within the void is then a function of the initial hydrogen concentration and the ambient temperature. Depending on these conditions, the pressure may be capable of inducing a stress which could exceed the level required to plastically strain the metal. Such strains may then nucleate microcavities which subsequently develop into blisters.^{30,32} In the decohesion model,²⁰ it is postulated that hydrogen dissolved in the steel in a region of a hydrostatic stress, weakens the cohesive forces that exist between the metal atoms, this may permit the nucleation of a micro-crack within the pre-formed plastic enclave²⁰ which then propagates back to join the primary crack front. After the advance of the primary crack, an incubation period would then follow in order to allow the diffusion of hydrogen to the new location of maximum tri-axial stress (i.e. the crack tip).²⁰ In the enhanced plasticity model, it is thought that the distribution of absorbed hydrogen in the steel is highly non-uniform in the

presence of an applied stress, thereby substantially reducing the flow stress of the steel.²² This results in a highly localized failure by ductile processes, while the total macroscopic deformation remains small. The general appearance of failures resulting from this model would appear as "brittle" due to the highly localized nature of the plasticity.²² The hydrogen embrittlement process is hypothesized to be a combination of several active mechanisms rather than one dominant mechanism.^{14,17,20,22,28,33} Based on this hypothesis, the particular mechanism ultimately responsible for failure by hydrogen embrittlement must be determined by the kinetics of the embrittlement system.²²

A typical time dependent process involves a combination of discrete steps or events in a sequence with the overall rate of progression being controlled by the slowest step. The embrittlement mechanisms proposed in the literature differ in the manner in which the environmental factors interact with strained metal to result in crack extension, but the mechanisms generally consist of: (1) transport of the environment to an existing crack tip, (2) reactions of the environment with newly created crack surfaces, (3) hydrogen entry (absorption), (4) diffusion of the hydrogen to the embrittlement zone, (5) redistribution of the hydrogen among available microstructural sites, (6) hydrogen-metal embrittlement reactions and finally (7) the separation process.^{14,29} Embrittlement has been shown to be related to microstructure.^{14,16,27} The extent of the embrittlement or the rate of crack extension along a microstructural element has been determined to be a function of the local hydrogen concentration which, in turn, has been shown to be dependent on the environmental conditions, specifically, the hydrogen fugacity and the ambient temperature.¹⁴ Any one of the steps in the sequence may be rate

determining since the environment has numerous influences on the growth rate of a crack and it is generally accepted that the environment at the tip of a propagating crack may differ significantly from the bulk environment.

Experiments were undertaken to evaluate the relative susceptibilities of the base metal and the weld HAZ's of HY-100 and HSLA-100 to hydrogen induced cold cracking. These experiments were designed to quantify the individual influences of welding parameters and alloy composition on the cracking behavior of both steels in an artificial seawater environment under controlled conditions, (e.g. hydrogen fugacity).

The range of potentials observed during the galvanic coupling of a steel to zinc in seawater is typically between -1.200V and -0.800V versus a saturated calomel reference electrode.³ In this potential range, the hydrogen fugacity may be sufficiently high so as to induce cracking in either alloy provided that a susceptible microstructure is present. The behaviors of both the base metal and a simulated weld HAZ of each alloy were thoroughly evaluated over this range of potentials in addition to conditions of extreme hydrogen fugacity and high corrosion rates.

EXPERIMENTAL

The objective of this study was to evaluate the cold cracking resistance of a HSLA-100 steel as compared to a typical HY-100 steel representative of the steels currently used for ship construction. To achieve this objective unambiguously, mechanical tests at fixed and reproducible hydrogen activities were required. Slow strain rate tensile tests were selected for the mechanical tests because of the strain rate dependence of hydrogen embrittlement and the activity of hydrogen on the surface of the samples was controlled by closed loop control of the potential difference between the sample and a reference electrode. To help with the interpretation of the results of these experiments, additional experiments were conducted to evaluate (1) the mechanical behavior of the base metal and the simulated weld HAZ of each alloy in an inert environment, (2) the electrochemical behavior of the base metal and the simulated HAZ of each alloy in the testing environment, (3) the relative susceptibilities of the base metal of the alloys to hydrogen embrittlement, (4) the microstructural differences between base metals and the HAZ's of the alloys and (5) the fracture morphology of the base metal and the simulated HAZ of each alloy.

The compositions of the HSLA-100 alloy and the HY-100 alloy selected for use in this study are given in Table 1. Cylindrical tensile specimens were machined from 25 mm (1 in) nominal thickness plate stock, supplied by the Annapolis Detachment of the Carderock Branch of the U.S. Naval Surface Warfare Center (NSWC) (formerly the David Taylor Research Center). All of the specimens were machined with the tensile axis parallel to the rolling direction.

Ten samples of both alloys were returned to NSWC-Annapolis for thermal cycling which was designed to simulate the HAZ created during a single pass welding operation. The temperature/time profile shown in Figure 2, is the control signal used by the weld zone emulator to generate the heat affected zones for this analysis. The temperatures were computer controlled remain within a range of ± 1.5 °C of the set point. The maximum temperature used for this simulation was nominally 1315 °C (2400 °F); the heat input was 55 kJoules, and the weld zone was preheated to 51.2 °C (125°F). Also, during the simulation process, the gauge section was shielded with argon to minimize oxidation effects. The samples were stored in a vacuum desiccator after heat treatment and/or machining prior to the onset of mechanical testing.

Slow strain rate tensile tests (SSR) were used to evaluate both the mechanical properties of hydrogen free material in an inert environment and the change in these properties when hydrogen is provided by electrochemical reactions on the surface. The intrinsic mechanical properties of the base metals and the simulated HAZ's of the alloys were determined by conducting SSR tests in dry nitrogen gas on samples which had been stored in a vacuum at room temperature for more than ninety days prior to testing. For the hydrogen source, it was decided to use an aqueous environment that would be commonly encountered in service. As a result, artificial seawater (ASTM Standard D1141-52) was used for this purpose rather than a highly buffered solution with a hydrogen recombination poison. Seawater is naturally buffered, but the solutions used in these tests were continuously recirculated and aerated with a peristaltic pump to minimize changes in the test environment during the test. The cell used

for the slow strain rate experiments is shown schematically in Figure 3. Approximately 1000 ml of solution was used for each test and the pH was measured before and after each test (ranging from 7.5 to 8.5 prior to testing, and from 6.0 to 9.5 after testing). For the constant potential (hydrogen fugacity) experiments, the potential of the sample was measured against a saturated calomel reference electrode ($0 V_{SCE} = 0.242 V_{NHE}$) and controlled with a commercial potentiostat. The mechanical tests were conducted using a computer controlled slow strain rate testing system which operated at a constant crosshead speed of $0.0254 \mu\text{m/sec}$ ($1 \times 10^{-6} \text{ in/sec}$). The computer system was configured to record applied load, crosshead displacement, elapsed time and either electrode potential or current depending on the particular experiment. Sample preparation for all of the tensile tests consisted of polishing the gauge section according to standard metallographic procedures. The remainder of the sample was coated with a stop-off lacquer to limit the surface area exposed to the environment. After failure, the samples were promptly removed from the cell, rinsed in flowing water and alcohol, dried and then stored in a vacuum desiccator until analyzed.

Electrodes were constructed from sections taken from SSR samples, mounted in epoxy and polished and used to evaluate the electrochemical behavior of the base metal and simulated HAZ's of the alloys. Two different types of experiments were used to characterize the electrochemical behavior of the base metal and the simulated HAZ's of the alloys in the artificial seawater environment: free corrosion potential measurements and potentiodynamic polarization experiments.

The free corrosion potential of the base metal and the simulated HAZ of each alloy was measured in naturally aerated and deaerated artificial seawater by placing the electrode along with a saturated calomel reference electrode (SCE) in an electrochemical cell connected to a computer controlled high impedance digital voltmeter. During the period required for the system to reach steady state, the measured potential and the elapsed time were recorded by the computer. Nitrogen was bubbled vigorously through the solution for twenty minutes to deaerate the seawater, after which, the flow rate was reduced and changed to a dispersion over the top of the solution surface.

The potentiodynamic polarization experiments were conducted by using a computer controlled potentiostat and a saturated calomel reference electrode. The potentiostat applies current to the sample to keep the potential difference between the sample and a reference electrode (SCE) equal to a predetermined value (E_d). For potentiodynamic polarization experiments, the potential, E_d , is not constant, but varies at a constant scan rate between selected extremes. For these experiments, the potential was scanned at 20mV/sec and 5mV/sec over a range of potentials designed to exceed those expected in normal service. Scans were also performed at the rate of 1mV/sec in order to resolve any possible features not observed at the higher scan rates. The method used for the 1mV/sec scans differed slightly from the previous scans in that the system was allowed to return to the steady state potential between the cathodic and anodic polarizations. A plot was then constructed from the two data segments.

Sections were cut from slow strain rate specimens for metallographic analysis in order to establish the base metal microstructure. The sections were

prepared according to standard metallographic procedure and then etched with CLQ-1, a solution specifically developed for low carbon steel microstructures, composed of 2 ml of a stock solution (100 ml H₂O, 100 ml HNO₃, and 15 ml (NH₄)₆Mo₇O₂₄•4H₂O) in 100 ml ethyl alcohol. Similar metallographic analyses were performed on lengthwise sections of the heat treated samples of both alloys in order to analyze the microstructural changes in the simulated HAZ.

Microhardness measurements were made along the length of the heat treated metallographic samples using a Vicker's indenter under a 500 gram load. This was done to quantify the changes in hardness as a function of distance away from the center of the simulated HAZ.

The fracture surfaces were cut from the broken SSR samples and prepared for analysis by immersion in a buffered descaling solution consisting of 3 ml HCl, 4 ml 2-Butyne 1,4-Diol (35% aq.) and 50 ml H₂O.³⁴ The reduction in area (RA) was determined from diameter measurements performed on the fracture surfaces with a optical measuring microscope prior to examination in a scanning electron microscope.

RESULTS

Slow strain rate tests

The results of the slow strain rate tests are presented in Tables 3 through 6. The ultimate tensile strength data (UTS) are plotted against the sample potential for both the base metal and the simulated HAZ of the HY-100 alloy in Figure 4a. A similar plot for the HSLA-100 alloy is shown in Figure 4b. No discernable trend is present in the UTS data for the HY-100. However, a slight increase in the strength was observed with decreasing potential in the HSLA-100 data. The strain to failure data, also plotted as a function of electrode potential and heat treatment, show a decrease in ductility with decreasing electrode potential for both conditions of the HY-100 alloy (Figure 5a) and the HSLA-100 alloy (Figure 5b). The strain to failure data for the HY-100 base metal ranged from a maximum value of 10.5 percent to a minimum value of 6.5 percent and the simulated HAZ ranged from 7.38 to 4.75 percent over the same potential range. The HSLA-100 strain to failure data also showed a comparable trend ranging from 12.5 percent to 7.0 percent for the base metal and from 8.1 percent to 4.0 percent in the simulated HAZ over the same potential range. The best illustration of the influence of hydrogen fugacity on the cracking resistance of the two alloys lies in the reduction in area (RA) data. In Figure 6a, both conditions of the HY-100 show a decrease in RA with electrode potential. A similar trend is also shown by both conditions of the HSLA-100 (Figure 6b). Through the range of potentials between $-0.800V_{s_{ce}}$ and $-1.200V_{s_{ce}}$, the base metal HY-100 showed a 35 percent decrease in the reduction in area data. A similar decrease in the RA data was observed in the simulated HAZ data. The reduction in the HSLA-100 data was comparable

showing approximately a 40 percent decrease for both the base metal and the simulated HAZ for the same potential range.

The strain to failure and the reduction in area graphs of Figures 5 and 6 can be divided into three regions based on their curvature. First, over a range of potentials the ductility observed in artificial seawater approaches that observed in nitrogen. This region is identified as "Region I" in Figure 6. Some decrease is observed for increasing potentials in this range, but this is due to dissolution reducing the cross section of the samples. Second, a region is observed over which the ductility changes rapidly with decreasing potential which is labeled as "Region II" in Figure 6. Third, a region is observed over which the rate of decrease in ductility with potential begins to decrease as shown in the area identified as "Region III" in Figure 6.

Electrochemistry

The measured free corrosion potentials for both alloys and heat treatments in static, aerated and deaerated artificial seawater are given in Table 2. Neither alloy demonstrated any significant differences in the steady state potentials between the base metal and the simulated HAZ conditions. Only small differences between the behavior of the base metal and the HAZ for the two alloys were observed. As shown in Figure 7a, the behaviors of the base metal and the simulated HAZ in aerated seawater are essentially the same. The base metal showed a slightly lower anodic current as the potential approached the transpassive region and this feature was also observed in deaerated seawater, as shown in Figure 7b. This suppression of the anodic current may reflect some

change in the surface film, but more likely, it reflects a change in the homogeneity of the microstructure. The behavior of the base metal and the simulated HAZ of the HSLA-100, shown in Figure 8a, were also very similar in the aerated seawater. Like the HY-100, subtle differences were observed between the two heat treatments and the same was true in the deaerated seawater, as shown in Figure 8b. Figures 9a and 9b show the electrochemical behaviors of two base metals and the two simulated HAZs for the alloys and these plots show that only small differences between the alloys were observed.

Microstructure

Quantitative metallography (QM) was performed on the base metal of the HY-100 and the HSLA-100 alloys to determine the size, shape and distribution of the inclusions present. Figures 10a and 10b are representative photomicrographs of the two alloys in the as polished condition and the results of the QM analysis are shown in Table 7. In general, the inclusions observed in the HY-100 alloy were larger in size, higher in number, and considerably less spherical than those observed in the HSLA-100 alloy.³⁵ The micrographs shown in Figure 11 represent the structures of the base metals of the alloys used in this analysis. The microstructure of the HY-100 base metal (Figure 11a) was identified as fine tempered lath martensite¹ and the HSLA-100 base metal (Figure 11b) was identified as coarse bainite with a random dispersion of incoherent niobium carbonitride precipitates.^{5,6} The microstructure of the simulated HAZ in HY-100 varied greatly over the length of the HAZ whereas the microstructural variations in the HSLA-100 simulated HAZ varied little. Figures 12a and 12b show the

microstructures in the HY-100 and the HSLA-100 simulated HAZ's which deviated the greatest from the structure of the base metal.

The variations in hardness as a function of distance from the center of the gauge section for both alloys are shown in Figures 13a and 13b. The HY-100 exhibited substantial changes in microhardness, ranging from approximately 264 VHN in the base metal to a maximum of 450 VHN in the simulated HAZ. The dashed lines in Figure 6 are extrapolations from the last measurements to the base metal hardness value and were included to illustrate the symmetry of the changes in observed in the hardness. The HSLA-100 exhibited microhardness values of approximately 270 VHN over the entire length of the base metal gauge section and increased to a maximum value of 320 VHN in the simulated HAZ.

Fractography

The fractographic analysis was in agreement with the trends observed in the slow strain rate data. The features observed on the fracture surfaces from Region I in Figure 6 were exclusively ductile in nature and consisted entirely of microvoid coalescence (MVC) and related features. In Region III, the region of lowest ductility in Figure 6, the features did include brittle cracking and while cracking was observed, it appeared to consist entirely of transgranular-like features. Intergranular cracking has been observed in these alloys, generally along the prior austenite grain boundaries,^{11,12} however, no features normally associated with cracking of this type were apparent on the surfaces of the fractures analyzed. The type of cracking observed on these fracture surfaces shall be referred to as transgranular cleavage-like (TCL) cracking. The features

observed in Region II, the transition region between Regions I and III in Figure 6, were generally a mixture of the two types of fracture: MVC and TCL.

Figures 14 and 15 are representative scanning electron micrographs from the HAZ's tested at the potentials in Region I. Figure 14a, a low magnification overview of the fracture surface of the HY-100, depicts the general characteristics observed on all of the fractures in this region (i.e. MVC surrounded by a large region of shear). Figure 14b is a high magnification view of the MVC region. Figure 15a is a low magnification overview of a HSLA-100 simulated HAZ from Region I and again shows the characteristic shear and MVC of fractures at the potentials in this region. A higher magnification view of the MVC observed in this alloy is shown in Figure 15b. Overall, the microvoids observed on the surfaces of the samples tested at the potentials in Region I indicated a good retention of ductility in both alloys.

Figures 16 and 17, show fracture surfaces of simulated HAZ samples of the two alloys tested at a potential within Region III. Figure 16a is an overview of a representative HY-100 fracture surface. None of the features normally associated with ductile fracture are present in this figure. Instead, the fracture surface is composed primarily of large TCL regions with secondary transgranular cracks. Figure 16b depicts the cracking observed in the HY-100 throughout this region. Figure 17a is a similar low magnification view of the HSLA 100 sample tested at a potential in Region III. Again, TCL cracking was observed, but this type of cracking was observed only near the edge of the fracture surface. The majority of the features on the HSLA-100 fracture surfaces in Region III was MVC. In Figure 17b, a high magnification view of the cracking observed and a transition

from the fine TCL features to MVC can be seen. Intergranular cracking was not observed on the fracture surfaces of either alloy.

Figures 18 and 19 are low magnification views of the two alloys in Region II and depict the general features observed on the surfaces. Figure 18 illustrates the mixed mode behavior of the HY-100 alloy HAZ. Small TCL cracks can be seen along the outer most edges in this figure, but the majority of the surface is MVC. Similar behavior was also observed on the HSLA-100 alloy surfaces in this region and they are represented in Figure 19.

The general behaviors observed in the base metals of both alloys in Region III are represented in Figures 20 and 21. The low magnification overview of Figure 20a illustrates the primarily TCL cracking observed in this region. Some small regions of MVC were observed. The generally finer cracking features observed in the base metal are depicted in the higher magnification view of Figure 20b. Similar behavior was demonstrated by the HSLA-100. Figures 21a and 21b are representative of the most severe cracking observed in the HSLA-100 samples in Region III.

DISCUSSION

The influences of electrode potential in a seawater environment on the mechanical properties of the HY-100 alloy and the HSLA-100 alloy were evaluated using the slow strain rate tensile test technique. The results (Table 3 through 6) showed that both alloys demonstrated good overall performance in the artificial seawater environment. This is illustrated in the plots of the individual mechanical properties versus the electrode potentials used in these experiments (Figures 11 and 12). The range of potentials expected in a zinc anode cathodic protection system in seawater is typically between $-1.200V_{sce}$ and $-0.800V_{sce}$. Therefore, attention should be paid to the mechanical performance of the two alloys in this potential range. The HSLA-100 alloy showed a slight trend toward increasing strength with decreasing electrode potential which may indicate some inhibition of dislocation motion by hydrogen. No similar trend could be discerned in the data for the HY-100 alloy. The base metal and the simulated HAZ of both alloys exhibited a trend toward decreasing strain to failure with decreasing electrode potential. The reduction in area plots illustrate marked decrease in the overall ductility of the base metals and simulated HAZ for both alloys as a function of decreasing electrode potential (Figures 12a and 12b). Using the average measured solution pH of 7.9, the hydrogen fugacity can be estimated for the different electrode potentials with the Nernst equation:

$$E(V_{SCE}) = -0.242 - 0.0296\{\log(P_{H_2})\} - 0.059[pH] \quad (4)$$

where E is the electrode potential in volts versus a saturated calomel reference electrode and P_{H_2} is the partial pressure of hydrogen. It should be noted that this equation assumes equilibrium and is valid only at equilibrium.³⁶

The electrochemical behavior of the two alloys was evaluated in order to characterize any differences that might influence the behavior in service. The free corrosion potentials of the two base metals and the two simulated HAZ were measured in artificial seawater. Since the free corrosion potential is a highly variable quantity, the resulting steady state values (Table 2) do not readily indicate any significant differences between the two base metals or between the two simulated HAZs in the artificial seawater environment. Subtle differences between the base metal and the simulated HAZ metal for both alloys were observed in the potentiodynamic scans (Figures 8 and 9). To further evaluate the presence of any electrochemical differences between the two alloys, the scans performed on the two base metals in deaerated solutions were plotted together (Figure 9a) and results demonstrated that the two base metals are very similar in behavior. The scans of two HAZs were plotted together (Figure 9b) and again no significant differences were observed. Based on these results, it was concluded that the electrochemical behavior of the two alloys and heat treatments were essentially the same. Therefore, any differences observed in the cracking resistance of the HY-100 and the HSLA-100 alloys can not be attributed to differences in their electrochemical behavior in this environment.

The finely dispersed tempered lath martensitic structure observed in the HY-100 alloy base metal (Figure 4a) was the microstructure anticipated for this alloy based on the carbon and chromium contents (0.2 percent and 1.6 percent,

respectively) and the subsequent quench and temper heat treatments used to achieve the strength and toughness levels. The HY-100 alloy composition included a relatively high sulfur content (0.013 percent) which may have produced the considerable number of large-sized inclusions observed in the QM analysis. The substantially lower sulfur content (0.0015 percent), combined with shape control elements, such as niobium, resulted in better distributed, more spherical inclusions in the HSLA-100 alloy. The coarse bainitic microstructure of this alloy included a random dispersion of incoherent precipitates (Figure 4b). The niobium carbonitride precipitates ranged in size which suggested a peak aged to a slightly overaged condition. The variations observed in the sizes of the prior austenite grains and the precipitates in the HSLA-100 alloy were minor and were probably due to the location of the sample in relation to the original plate thickness.

The microstructures in the simulated weld HAZ of the HY-100 alloy demonstrated the wide variations expected for a steel with a relatively high degree of hardenability (Zone III in Figure 1)⁹. The microstructures observed along the length of the gauge section in the HY-100 alloy fell into four groups ranging from extremely fine structures, found in the regions surrounding the contact points of the weld simulator, to the largest structures found in the central region of the gauge section (Figure 5a). The HSLA-100 alloy, a steel with a relatively flat hardenability curve (Zone I in Figure 1)⁹, exhibited little variation in microstructure along the length of the gauge section. The microstructural variations observed in this alloy were primarily in the appearance of the precipitates and the coarseness of the prior austenite grains. At the contact areas, the microstructures were much finer than those observed in the base metal

and the precipitates were not visible at low magnifications. This suggests a possible resolutionizing of the niobium precipitates in this region. In the central region of the gauge section, the prior austenite grain size was much larger than that observed in the base metal and the precipitates were not readily visible (Figure 5b).

The changes in hardness and the corresponding variations in microstructure for the two alloys are best illustrated when plotted as a function of distance from the center of the gauge section. As expected, the higher carbon content with its influence on the hardenability in the HY-100 alloy produced large increases in the hardness throughout the entire HAZ. The microhardness values for this alloy increased by approximately 70 to 75 percent over the length of the gauge section (Figure 6a). This large increase in hardness appears to be due to the observed increase in the coarseness of the martensite colonies. The changes in hardness observed in the HSLA-100 alloy were considerably smaller in magnitude than those observed in the HY-100 alloy (Figure 6b). The 20 percent increase observed in the microhardness values of the HSLA-100 was expected because of the low hardenability composition of this alloy. The substantial changes generated in the microstructures and hardness levels in the HY-100 alloy for the simulated welding condition used in this analysis suggest that this alloy is likely to produce one or more microstructures which could be highly susceptible to hydrogen embrittlement since the general tolerance of a microstructure to hydrogen is thought to be inversely proportional to the hardenability of the steel.¹⁰

The fractographic analysis of the base metal and the simulated HAZs of the two alloys revealed pronounced changes in the fracture surface morphologies which was in agreement with the observed decreases in ductility. The observed morphologies ranged from completely ductile MVC at cathodic electrode potentials between 0 and 200mV (Figures 14 and 15) to TCL at cathodic potentials greater than 300mV (Figures 16 and 17). In general, the TCL cracking observed on the base metal fracture surfaces was generally finer in appearance at the low electrode potentials as opposed to the cracks observed on the simulated weld zone heat treated surfaces at the same potentials (Figures 20 and 21).

In the range of potentials anticipated in service, the HY-100 alloy demonstrated a trend toward decreasing ductility with decreasing electrode potential. The HSLA-100 alloy exhibited a similar progressive decrease in the ductility with decreasing potential over the same range of potentials, but the loss in ductility reached a plateau value of approximately 25 to 30 percent reduction in area after which no further reduction in ductility was observed. This indicates that the ductility of the HSLA-100 alloy should not continue to decrease with decreasing electrode potentials. The trend toward a minimum ductility value was not observed in the HY-100 alloy. This suggests that either a plateau region similar to the one observed in the HSLA-100 alloy may form at potentials lower than those included in this evaluation or that the hydrogen embrittlement effect became saturated in the HSLA-100 alloy at -1.200Vsce. Further examination of the behavior of the HY-100 alloy at extremely low electrode potentials (<-1.400Vsce) is required to verify the presence of a minimum ductility value.

The results of this evaluation demonstrate that the HY-100 and the HSLA-100 alloys have similar mechanical properties and electrochemical behaviors. The HY-100 alloy utilizes high carbon and chromium contents to obtain a degree of hardenability suitable to produce a steel with high strength and toughness through appropriate quench and temper operations. The large increase in hardness observed in a simulated weld HAZ in this alloy corresponded to microstructural variations which, in turn, could indicate the formation of microstructures which are more susceptible to hydrogen induced cold cracking. The HSLA-100 alloy has a low carbon content and utilizes precipitation hardening to obtain strengths and toughnesses similar to the HY-100 alloy. As a result of the lower carbon content, the hardenability in the weld zone is substantially reduced for the HSLA steel. The observed changes in hardness and microstructure in a simulated weld HAZ in the HSLA alloy were considerably smaller than those observed in the HY-100 alloy which indicated that the HSLA-100 alloy was less likely to produce microstructures susceptible to hydrogen induced cold cracking. The inclusions observed in the HY-100 were generally larger, higher in number and considerably less spherical than those observed in the HSLA-100 alloy. This is a result of the substantially higher sulfur content and the lack of shape control elements in the HY-100 alloy. Over the range of potentials anticipated in a cathodic protection system with a zinc anode, both alloys demonstrated good ductility, and resistance to hydrogen induced cracking, but at extreme hydrogen fugacities, the HY-100 demonstrated a trend toward more pronounced embrittlement, whereas in the HSLA-100 alloy, a plateau in ductility was observed indicating no further loss of ductility with

increased hydrogen fugacity. Based on this result, it would appear that the simulated HAZ of the HSLA-100 was generally less susceptible to hydrogen induced cracking than the simulated weld zone of the HY-100. Since the base metals and the simulated HAZs of the two alloys demonstrated essentially the same behavior in the artificial seawater, the noticeable differences in the susceptibilities at high hydrogen fugacities cannot readily be attributed to differences in the electrochemical behaviors in this environment.

It would also appear that the higher carbon martensitic structure of the HY-100 is more susceptible to hydrogen induced cold cracking in the simulated weld zone than the lower carbon bainitic precipitation hardened structures of the HSLA-100 alloy. This may be due to the substantially finer and more dispersed inclusions observed in the HSLA-100 alloy. Finer, well distributed inclusions have previously been shown to improve the resistance of a low carbon steel to hydrogen embrittlement and to reduce the stress concentration at the inclusion-matrix interface which, in turn, increases the plastic deformation at the tip of a propagating brittle crack. The observed minimum ductility in this alloy may be a result of these effects. Further evaluation of the relationships between the microstructural differences, inclusions and hydrogen trapping effects in these two alloys is required.

Based on these results, it may be concluded that the variations observed in the martensitic structure and the associated increases in hardness produced during a simulated welding operation, strongly influenced the behavior of the HY-100 alloy in the artificial seawater environment whereas the microstructures produced by the HSLA-100 alloy under the same simulated welding conditions

appeared to be less susceptible to hydrogen induced cold cracking. While the two alloys were similar in mechanical and electrochemical performance, the cleaner, lower carbon, HSLA-100 alloy was more effective in resisting cold cracking in the simulated weld heat affected zone than the HY-100 alloy over the range of potentials evaluated.

CONCLUSIONS

The purpose of this evaluation was to characterize the susceptibilities of two alloys with similar yield stresses to cold cracking in simulated weld heat affected zones. The first alloy, HY-100, contained moderate carbon and chromium contents and possessed a quenched and tempered martensite microstructure. This generated a high degree of hardenability which produced large variations in microstructure and hardness in a simulated weld HAZ. The second alloy, HSLA-100 a very low carbon, bainitic structure, utilized copper and niobium carbonitride precipitation to achieve similar strength and toughness levels. The degree of hardenability produced in this alloy was substantially lower than that of the HY-100 and minimal variations in microstructure and hardness were observed in a simulated HAZ.

The mechanical properties of the base metal and a simulated weld HAZ were evaluated for each alloy in an inert environment and in an artificial seawater environment under free corrosion and at controlled potentials. The electrochemical behaviors were also characterized in the artificial seawater environment in order to determine whether any differences in the susceptibility could be due to the corrosion behavior of the alloys. The results of these evaluations indicated that the mechanical and the electrochemical behaviors of both alloys are very similar in artificial seawater environment especially in the range of potentials expected in service. A slight difference between the two alloys was observed in the ductility data. At high hydrogen fugacities, the ductility in the HSLA-100 steel approached a minimum value. The HY-100 alloy did not

exhibit a similar trend. This is believed to be due to the presence of a more susceptible microstructure produced in the simulated weld HAZ in the HY-100 alloy. However, further analysis is required to determine whether a similar plateau is present at potentials lower than those included in this evaluation. These results were supported by the fractography. The transgranular cleavage-like cracks observed on the fracture surface of the HY-100 alloy were generally larger and higher in number than those observed on the HSLA-100 alloy tested at the same hydrogen fugacity. No distinct intergranular cracking was observed in either alloy or heat treatment. Analysis of the microstructures revealed a substantially high content of large inclusions in the HY-100 alloy whereas the inclusions present in the HSLA-100 were much finer, more uniform in shape and more dispersed. Micro-hardness measurements in the HAZs revealed a 70 percent increase in hardness of the HY-100 while the increase in the HSLA-100 was only 20 percent.

The results of this evaluation indicated that while the two alloys were similar in strength and electrochemical behaviors in the artificial seawater environment, the simulated weld HAZ of the HSLA-100 alloy was generally less susceptible to hydrogen induced cold cracking than the HY-100 alloy. Since the electrochemical data were essentially the same, the observed differences in the susceptibilities can not be attributed to differences in the electrochemical behavior. Therefore, it was concluded that the increased susceptibility to cold cracking observed in the HY-100 steel was a result of the variability of the martensitic microstructure and the influences of inclusions present. The size and distribution of inclusions contained in a particular steel are known to have a

strong influence on the susceptibility to hydrogen embrittlement and on the degree of stress concentration and plastic deformation at the matrix-inclusion interface. Therefore, further analysis to determine the influences of microstructure, inclusion size, shape and distribution, hydrogen trap density and diffusion rates on the relative susceptibilities to hydrogen induced cold cracking in these two alloys is needed and is in progress.

The performance of the HSLA-100 alloy was equal or superior to that of the HY-100 in all cases over the range of potentials examined in this study. The HSLA-100 alloy demonstrated a higher resistance to cracking and a better retention of ductility at high hydrogen fugacities than the HY-100 alloy.

ACKNOWLEDGEMENT

The authors would like to thank Dr. J. P. Gudas and Mr. G. E. Hicho for their numerous suggestions and helpful discussions, Mr. J. L. Fink and Mr. L. C. Smith for their technical assistance and Dr. M. Vassilaros of the NSWC-Annapolis for supplying the materials used in this evaluation. The authors would also like to acknowledge the financial support of the U. S. Office of Naval Research, contract No. N00014-89-F-0101, under the supervision of Dr. A. K. Vasudevan.

REFERENCES

1. H. E. McGannon, "The Making, Shaping and Treating of Steel," The United States Steel Corporation, (1971), 1420.
2. W. F. Smith, Structure and Properties of Engineering Alloys, McGraw-Hill Book Company, (1981).
3. E. J. Czyryca, et al., "Development and Certification of HSLA-100 Steel for Naval Ship Construction," Naval Engineers Journal, 102, (1990), 63-82.
4. E. J. Czyryca, "Development of Low-Carbon, Copper Strengthened HSLA Steel Plate for Naval Ship Construction," DTRC-SME-90/21, David Taylor Research Center, (1990).
5. A. D. Wilson, et al., "Properties and Microstructures of Copper Precipitation Aged Plate Steels," Microalloyed HSLA Steels, ASM International, (1988), 259-275.
6. M. T. Miglin, et al., "Microstructure of a Quenched and Tempered Cu-Bearing High Strength Low Alloy Steel," Metall Trans A, 17A, (1986), 791-798.
7. R. A. DePaul and A. L. Kitchin, "The Role of Nickel, Copper, and Columbium (Niobium) in Strengthening a Low Carbon Ferritic Steel," Metall Trans A, 1, (1970), 389-393.
8. A. B. Rothwell, "Weldability of HSLA Structural Steels," Metalls Prog., 111, (1977), 43-50.
9. B. A. Graville, "Cold Cracking in Welds in HSLA Steels," Weld Des & Fab, (1979), 57-61.
10. B. A. Graville, The Principles of Cold Cracking Control in Welds, Dominion Bridge Company, (1975).
11. G. R. Hoey, R. R. Ramsingh and J. T. Bowker, "Dependence of Stress Corrosion Cracking of Parent, Heat-Affected Zone, and Weld Metal of HSLA Line-Pipe Steel on Potential," Corrosion Monitoring in Industrial Plants Using Nondestructive Testing and Electrochemical Methods, G. C. Moran and P. Labine, ASTM, (1984), 386-403.

12. R. W. Revie and R. R. Ramsingh, "Effects of Potential on Stress-Corrosion Cracking of Grade 483 (X-70) HSLA Line-Pipe Steels," Can. Metall Quarter, 22, (1983), 235-240.
13. D. A. Ryder, T. Grundy and T. J. Davies, "The Effect of the Microstructure of Steel On Susceptibility to Hydrogen Embrittlement," Current Solutions to Hydrogen Problems in Steels, C. G. Interrante and G. M. Pressouyre, American Society for Metals, (1982), 272-274.
14. R. P. Wei and M. Gao, "Hydrogen Embrittlement and Environmentally Assisted Crack Growth," Hydrogen Effects on Material Behavior, N. R. Moody and A. W. Thompson, The Minerals, Metals & Materials Society, (1990), 789-813.
15. P. A. Klein and R. A. Hays, "The Hydrogen Cracking Initiation Susceptibility of HY-130 Steel Base Plates and Weldments in Marine Environments," DTRC-SME-89/83, David Taylor Research Center, (1989).
16. I. M. Bernstein and A. W. Thompson, "The Role of Microstructure in Hydrogen Embrittlement," Hydrogen Embrittlement and Stress Corrosion Cracking, American Society for Metals, (1980), 135-152.
17. A. W. Thompson, "Effect of Metallurgical Variables on Environmental Fracture of Engineering Materials," Environment-Sensitive Fracture of Engineering Materials, Z. A. Foroulis, The Metallurgical Society of AIME, (1977), 379-410.
18. H. H. Johnson, "Hydrogen in Iron," Metall Trans A, 19A, (1988), 2371-2387.
19. M. F. Fernandes, "Hydrogen Absorption and Embrittlement of Rare Earth Modified 2 1/4 Cr-1 Mo Steels," PhD, University of Notre Dame, (1989).
20. R. A. Oriani, "Hydrogen-- The Versatile Embrittler," Corro, 43, (1987), 390-397.
21. M. F. Stevens and I. M. Bernstein, "Microstructural Trapping Effects on Hydrogen Induced Cracking of a Microalloyed Steel," Metall Trans A, 20A, (1989), 909-919.
22. H. K. Birnbaum, "Mechanisms of Hydrogen Related Fracture of Metals," Hydrogen Effects on Material Behavior, N. R. Moody and A. W. Thompson, The Minerals, Metals & Materials Society, (1990), 639-658.
23. R. M. Latanision, O. H. Gastine and C. R. Compeau, "Stress Corrosion Cracking and Hydrogen Embrittlement: Differences and Similarities," Environment-Sensitive Fracture of Engineering Materials, Z. A. Foroulis, The Metallurgical Society of AIME, (1977), 48-70.

24. I. M. Bernstein, et al., "Microstructural Control of Hydrogen Embrittlement in Steels," Current Solutions to Hydrogen Problems in Steels, C. G. Interrante and G. M. Pressouyre, ASM, (1982), 259-262.
25. M. I. Luppó and J. Ovejero-Garcia, "The Influence of Microstructure on the Trapping and Diffusion of Hydrogen in a Low Carbon Steel," Corro Sci, 32, (1991), 1125-1136.
26. G. R. Speich and W. C. Leslie, "Tempering of Steel," Metall Trans, 3, (1972), 1043-1054.
27. R. Kerr, et al., "Microstructural Effect on the Stress Corrosion Cracking Behavior of Medium and High Strength Steels," Metall Trans A, 18A, (1987), 1011-1022.
28. J. P. Hirth, "Hydrogen Influenced Plastic Instability and Ductile Fracture in Steels," Hydrogen Effects on Material Behavior, N. R. Moody and A. W. Thompson, The Minerals, Metals & Materials Society, (1990), 677-685.
29. R. E. Ricker and D. J. Duquette, "The Role of Environment on Time Dependent Crack Growth," Micro and Macro Mechanics of Crack Growth, K. Sadananda, B. B. Rath and D. J. Michel, TMS, (1981), 29-47.
30. M. R. Louthan, "The Effect of Hydrogen on Metals," Corrosion Mechanisms, F. Mansfeld, Marcel Dekker, (1987), 329-365.
31. C. F. Barth and E. A. Steigerwald, "Evaluation of Hydrogen Embrittlement Mechanisms," Metall Trans, 1, (1970), 3451-3455.
32. C. Zapffe, Trans. ASM, 39, (1947), 191.
33. H. J. Maier and H. Kaeshe, "Aspects of Hydrogen Effects on Fracture Processes," Hydrogen Effects on Material Behavior, N. R. Moody and A. W. Thompson, The Minerals, Metals & Materials Society, (1990), 733-742.
34. "Proceedings of the Scanning Electron Microscopy Workshop," (1974), 94.
35. G. F. VanderVoort, "Quantitative Metallography," Metallography Principles and Practice, McGraw-Hill Inc, (1984), 410-502.
36. R. E. Ricker, M. R. Stoudt and J. L. Fink, "Hydrogen Embrittlement of Ductile Nickel Aluminide During Corrosion in Aqueous Solutions," Hydrogen Effects on Material Behavior, N. R. Moody and A. W. Thompson, TMS, (1990), 499-506.

Table 1 Chemistries of the Two High Strength Steel Alloys

| | <u>HY-100</u> | <u>HSLA-100</u> |
|------------|---------------|-----------------|
| Carbon | 0.16 | 0.015 |
| Manganese | 0.25 | 0.95 |
| Nickel | 2.94 | 3.55 |
| Molybdenum | 0.43 | 0.61 |
| Chromium | 1.59 | 0.61 |
| Vanadium | 0.005 | --- |
| Aluminum | --- | 0.054 |
| Copper | 0.05 | 1.71 |
| Niobium | --- | 0.044 |
| Silicon | 0.23 | 0.38 |
| Phosphorus | 0.009 | 0.008 |
| Sulfur | 0.013 | 0.0015 |

Table 2. Free Corrosion Potentials Measured in ASTM Artificial Seawater

| <u>Alloy</u> | <u>Condition</u> | <u>Aeration</u> | <u>Free Corrosion Potential (Vsce)</u> |
|--------------|------------------|-----------------|--|
| HY-100 | Parent Metal | Aerated | -0.650 |
| HY-100 | HAZ | Aerated | -0.635 |
| HY-100 | Parent Metal | Deaerated | -0.740 |
| HY-100 | HAZ | Deaerated | -0.730 |
| | | | |
| HSLA-100 | Parent Metal | Aerated | -0.640 |
| HSLA-100 | HAZ | Aerated | -0.660 |
| HSLA-100 | Parent Metal | Deaerated | -0.730 |
| HSLA-100 | HAZ | Deaerated | -0.725 |

Table 3 Mechanical Properties of HY-100 Parent Metal

| <u>Testing Environment</u> | <u>Potential (V_{sce})</u> | <u>Ultimate Tensile Stress (MPa)</u> | <u>Total Strain to Failure (percent)</u> | <u>Reduction in Area (percent)</u> |
|----------------------------|------------------------------------|--------------------------------------|--|------------------------------------|
| Nitrogen | None | 799.90 | 10.63 | 68.98 |
| Seawater | Eoc | 780.08 | 10.03 | 67.45 |
| Seawater | -0.600 | 797.82 | 10.38 | 69.07 |
| Seawater | -0.800 | 800.66 | 9.40 | 66.60 |
| Seawater | -0.900 | 810.01 | 9.20 | 63.57 |
| Seawater | -1.000 | 785.25 | 9.25 | 55.83 |
| Seawater | -1.200 | 801.34 | 7.02 | 43.61 |
| Seawater | -1.400 | 814.90 | 6.55 | 35.41 |

**Table 4 Mechanical Properties of HY-100
Simulated Weld Heat Affected Zone**

| <u>Testing Environment</u> | <u>Potential (V_{sce})</u> | <u>Ultimate Tensile Stress (MPa)</u> | <u>Total Strain to Failure (percent)</u> | <u>Reduction in Area (percent)</u> |
|--------------------------------|--|--|--|--|
| Nitrogen | none | 865.83 | 7.38 | 61.62 |
| Seawater | E _{oc} | 819.47 | 7.19 | 59.71 |
| Seawater | -0.550 | 826.22 | 6.45 | 64.08 |
| Seawater | -0.800 | 808.37 | 6.84 | 62.51 |
| Seawater | -1.000 | 821.30 | 5.93 | 47.54 |
| Seawater | -1.200 | 816.36 | 4.77 | 39.53 |

Table 5 Mechanical Properties of HSLA-100 Parent Metal

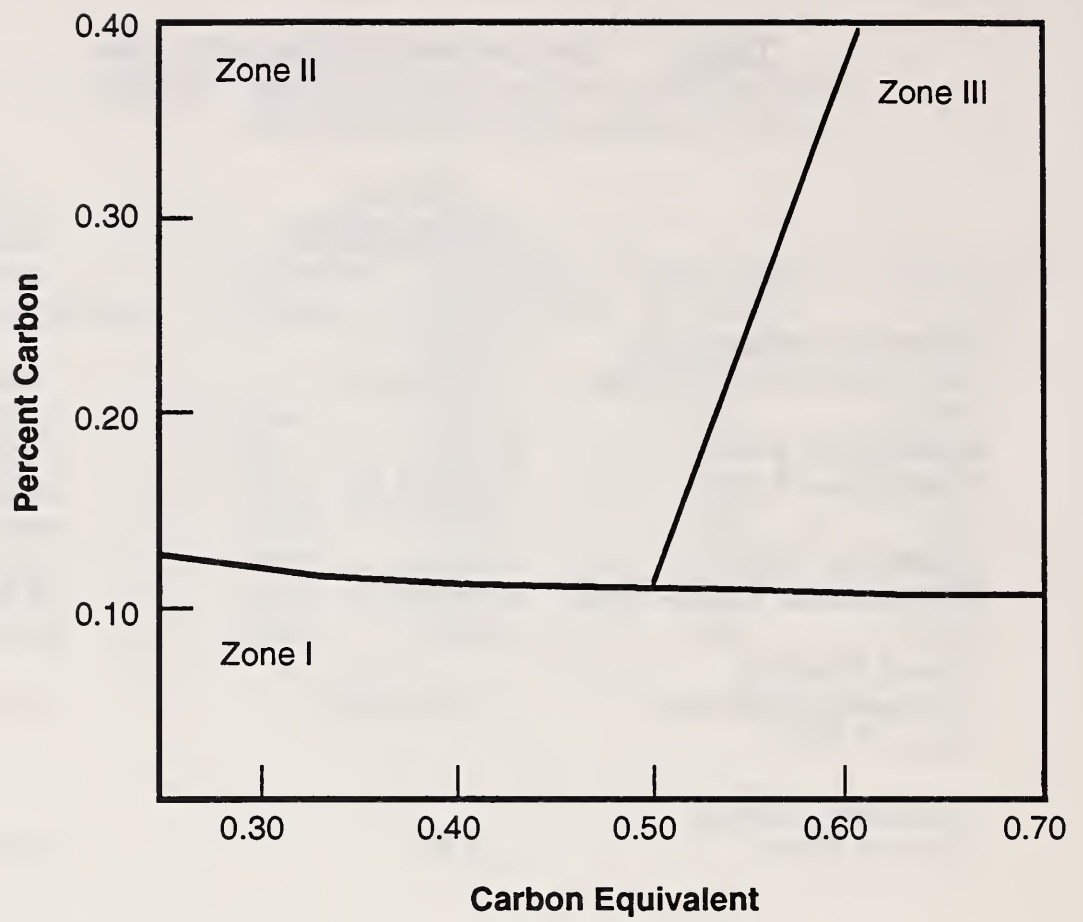
| <u>Testing Environment</u> | <u>Potential (V_{sce})</u> | <u>Ultimate Tensile Stress (MPa)</u> | <u>Total Strain to Failure (percent)</u> | <u>Reduction in Area (percent)</u> |
|----------------------------|------------------------------------|--------------------------------------|--|------------------------------------|
| Nitrogen | None | 739.12 | 12.26 | 80.52 |
| Seawater | Eoc | 747.98 | 12.65 | 78.97 |
| Seawater | -0.500 | 683.26 | 11.32 | 79.17 |
| Seawater | -0.600 | 737.62 | 12.45 | 80.92 |
| Seawater | -0.800 | 750.76 | 12.49 | 80.81 |
| Seawater | -0.900 | 754.13 | 11.99 | 69.61 |
| Seawater | -1.000 | 756.25 | 10.78 | 42.93 |
| Seawater | -1.200 | 763.48 | 7.01 | 28.00 |
| Seawater | -1.400 | 757.16 | 7.45 | 28.15 |

Table 6 Mechanical Properties of HSLA-100
Simulated Weld Heat Affected Zone

| <u>Testing Environment</u> | <u>Potential (V_{sce})</u> | <u>Ultimate Tensile Stress (MPa)</u> | <u>Total Strain to Failure (percent)</u> | <u>Reduction in Area (percent)</u> |
|--------------------------------|--|--|--|--|
| Nitrogen | none | 797.39 | 6.71 | 88.90 |
| Seawater | E _{oc} | 764.42 | 7.90 | 82.29 |
| Seawater | -0.600 | 751.05 | 8.16 | 92.43 |
| Seawater | -0.800 | 757.67 | 8.10 | 77.80 |
| Seawater | -1.000 | 766.95 | 6.55 | 59.50 |
| Seawater | -1.200 | 766.42 | 4.76 | 33.10 |
| Seawater | -1.400 | 765.58 | 3.94 | 35.35 |

Table 7 Quantitative Metallography Data

| | <u>HY-100</u> <u>Parent Metal</u> | <u>HSLA-100</u> <u>Parent Metal</u> |
|--|--------------------------------------|--|
| Prior Austenite Grain Size (μm) @ 250x | 19.4 ± 8.4 | 36.4 ± 11.3 |
| Inclusions per Unit Area @ 250x | 72.0 ± 5.6 | 18.9 ± 1.8 |
| Inclusion Size Distribution (μm) @ 500x | 9.3 ± 6.3 | 1.9 ± 1.4 |
| Mean Spacing Between Inclusions (μm) @ 250x | 65.2 ± 37.6 | 175 ± 105 |
| Inclusion Aspect Ratio @ 500x | 0.17 | 1.00 |



$$CE = C + \frac{Mn}{6} + \frac{Si}{7} + \frac{Ni}{55} + \frac{Cr}{5} + \frac{Mo}{4} + \frac{V}{5} + 1.3Nb$$

Figure 1 The relationship between the actual carbon content, the carbon equivalent and the susceptibility to hydrogen induced cold cracking.⁹

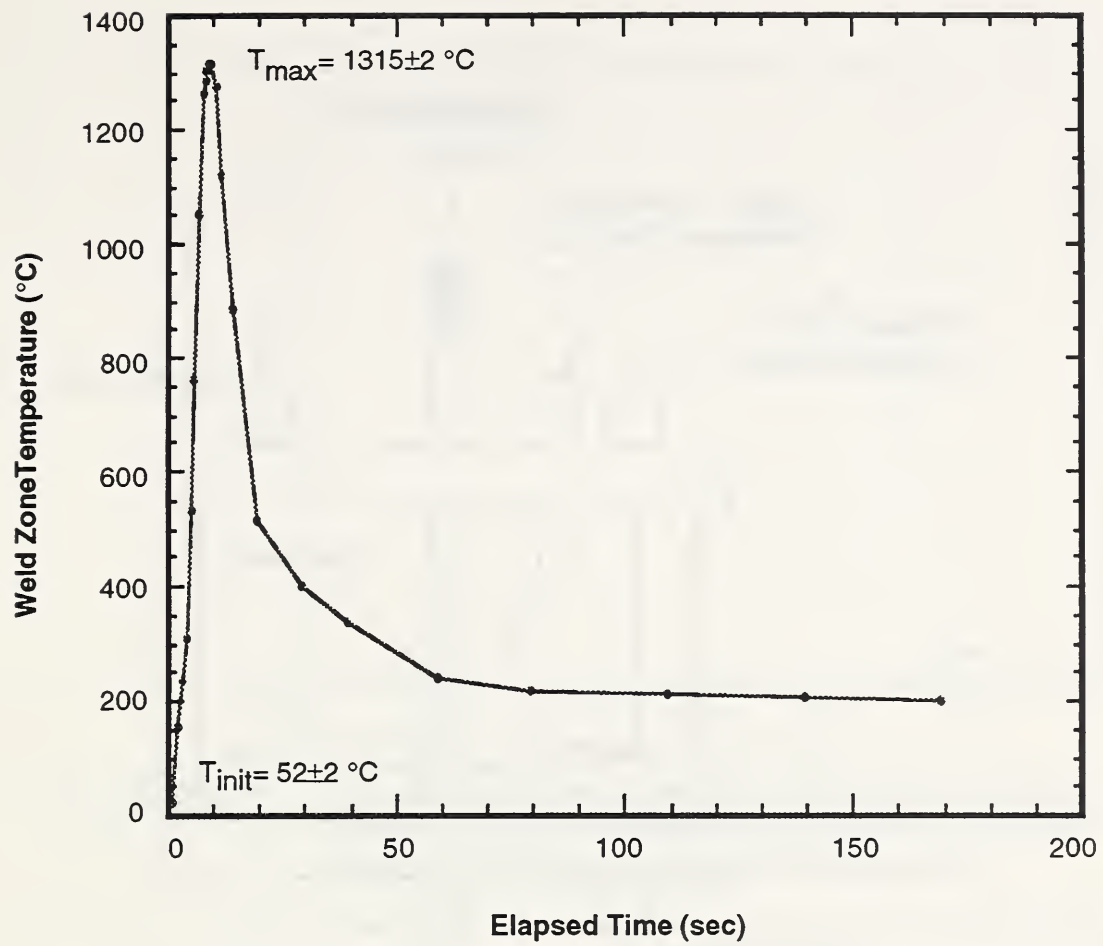


Figure 2 The temperature-time command profile used to create the simulated heat affected zone resulting from a single welding pass.

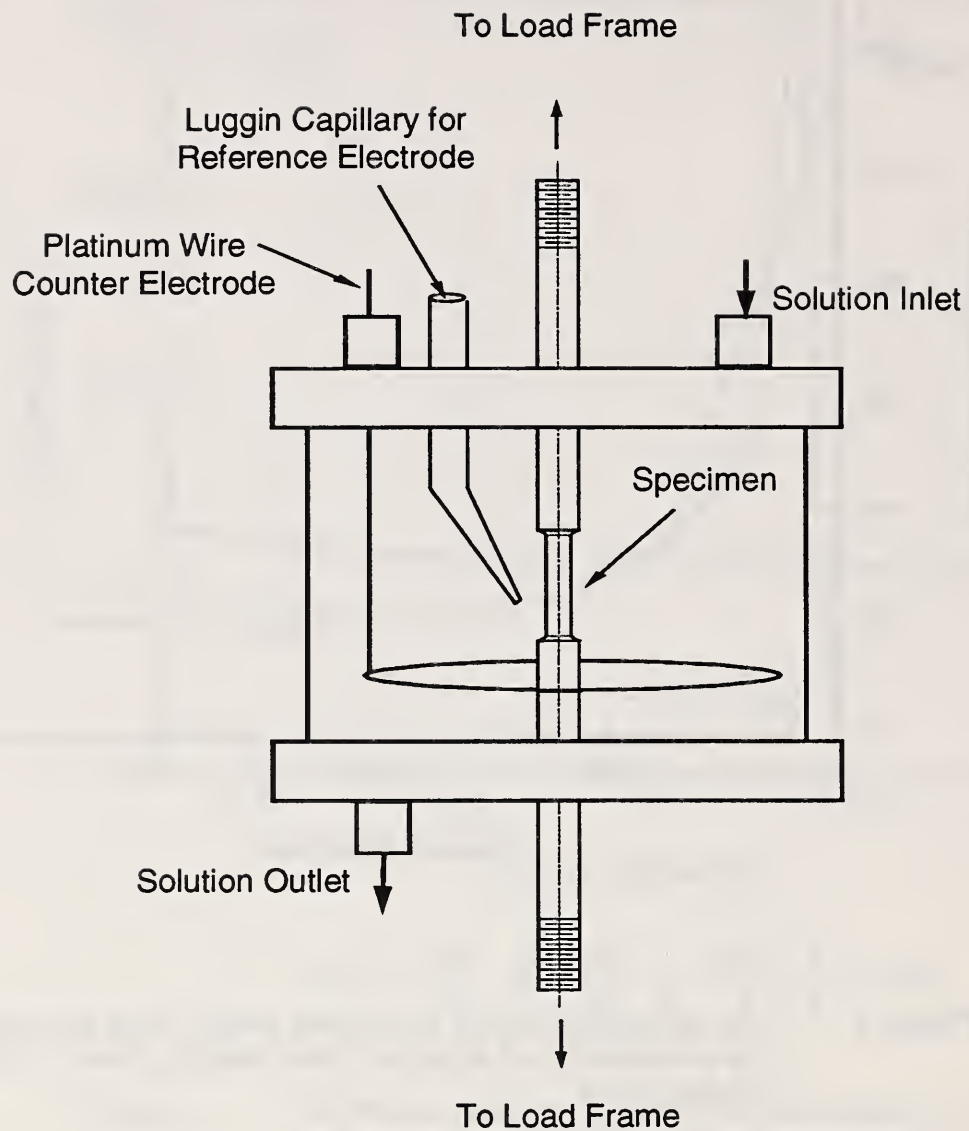


Figure 3 A schematic diagram of the electrochemical cell used in the slow strain rate tests.

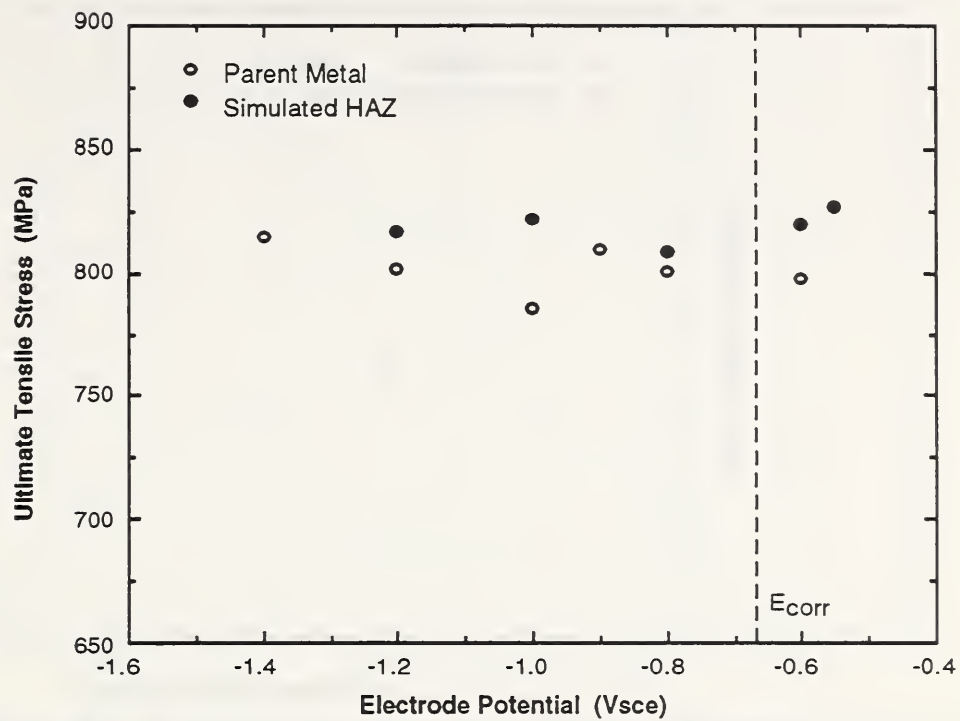


Figure 4a The ultimate tensile strength vs electrode potential for the HY-100 parent metal and simulated heat affected zone in recirculating ASTM artificial seawater.

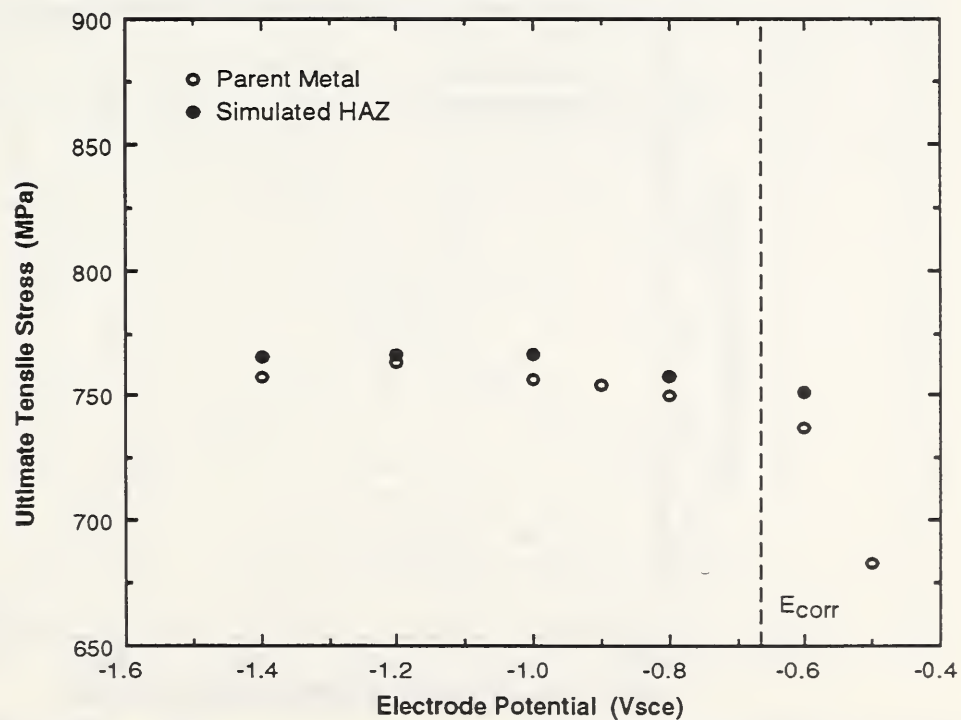


Figure 4b The ultimate tensile strength vs electrode potential for the HSLA-100 parent metal and simulated heat affected zone in recirculating ASTM artificial seawater.

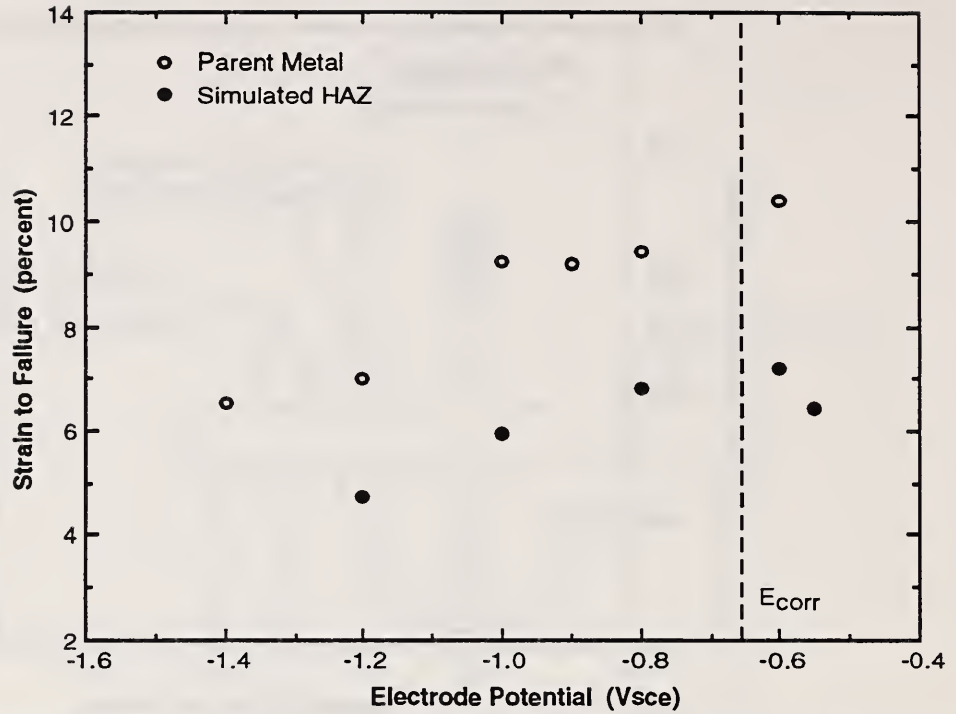


Figure 5a The strain to failure vs electrode potential for the HY-100 parent metal and simulated heat affected zone in recirculating ASTM artificial seawater.

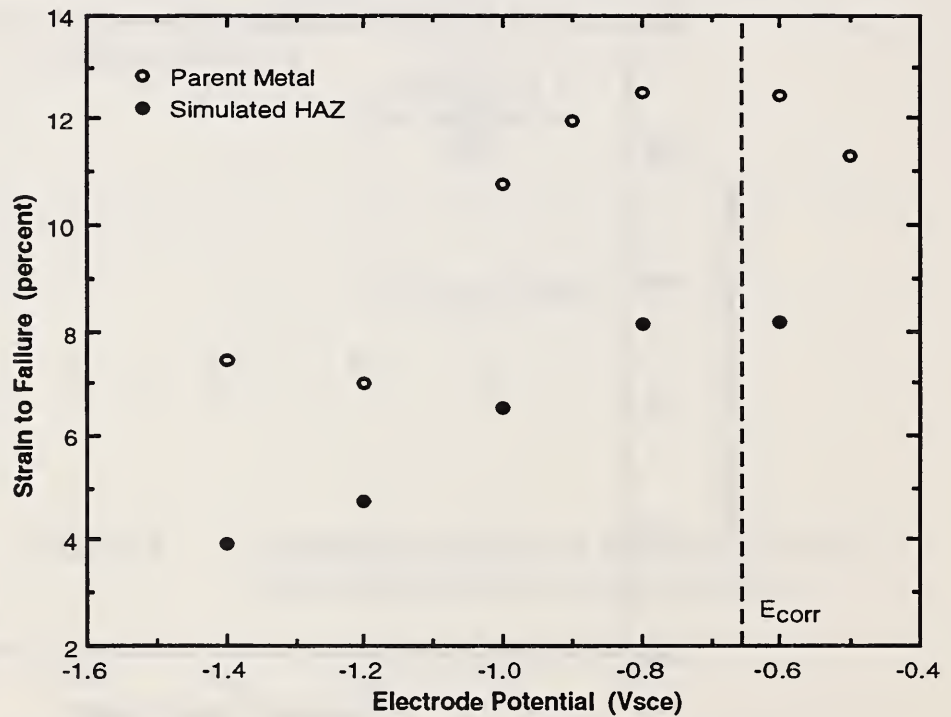


Figure 5b The strain to failure vs electrode potential for the HSLA-100 parent metal and simulated heat affected zone in recirculating ASTM artificial seawater.

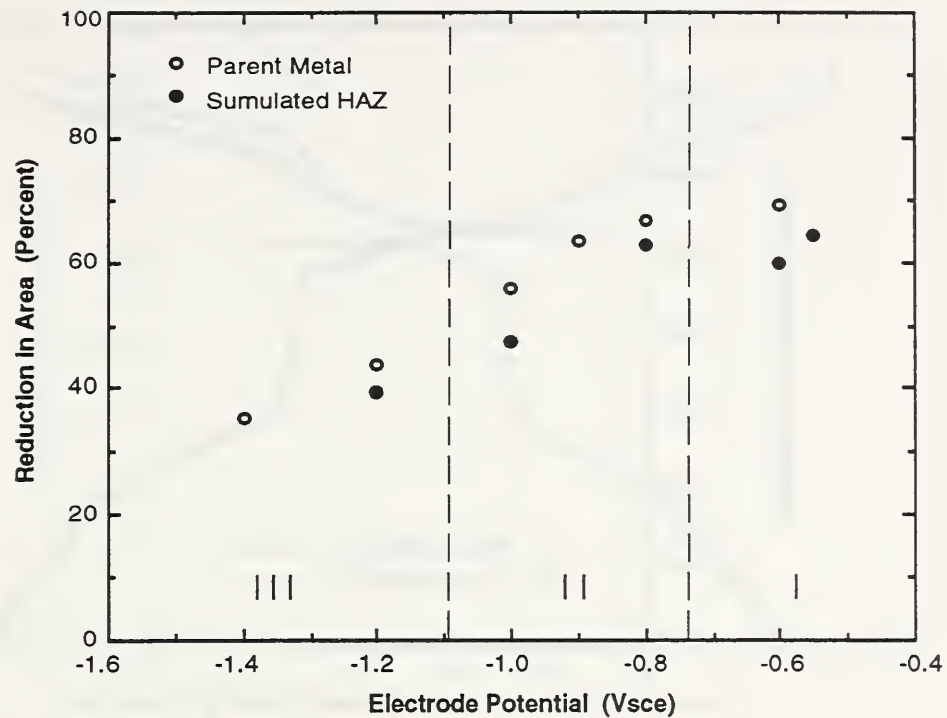


Figure 6a The reduction in area vs electrode potential for the HY-100 parent metal and simulated heat affected zone in recirculating ASTM artificial seawater.

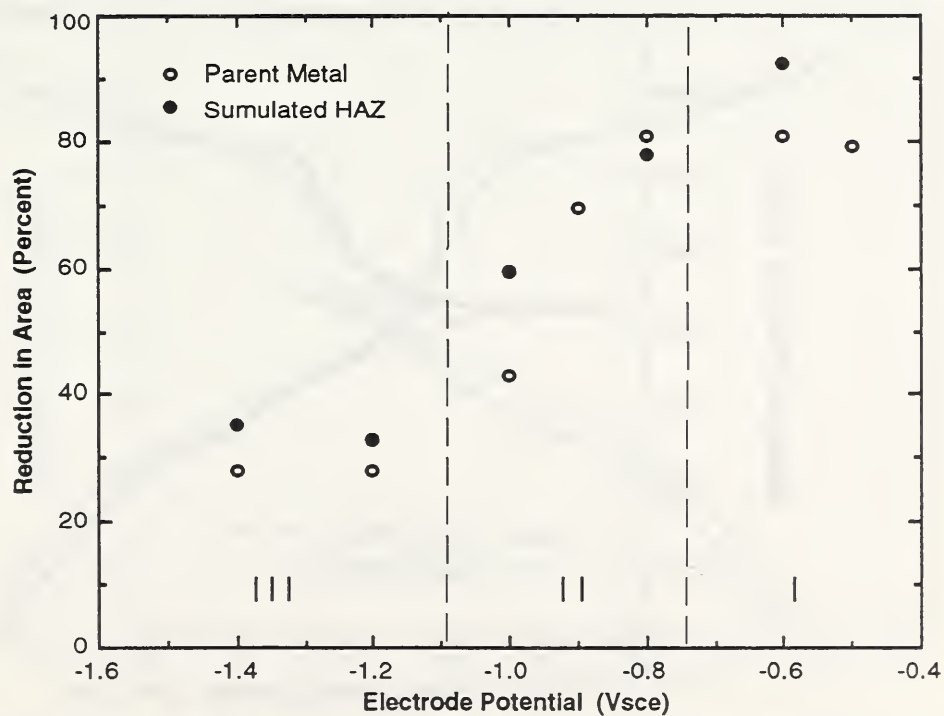


Figure 6b The reduction in area vs electrode potential for the HSLA-100 parent metal and simulated heat affected zone in recirculating ASTM artificial seawater.

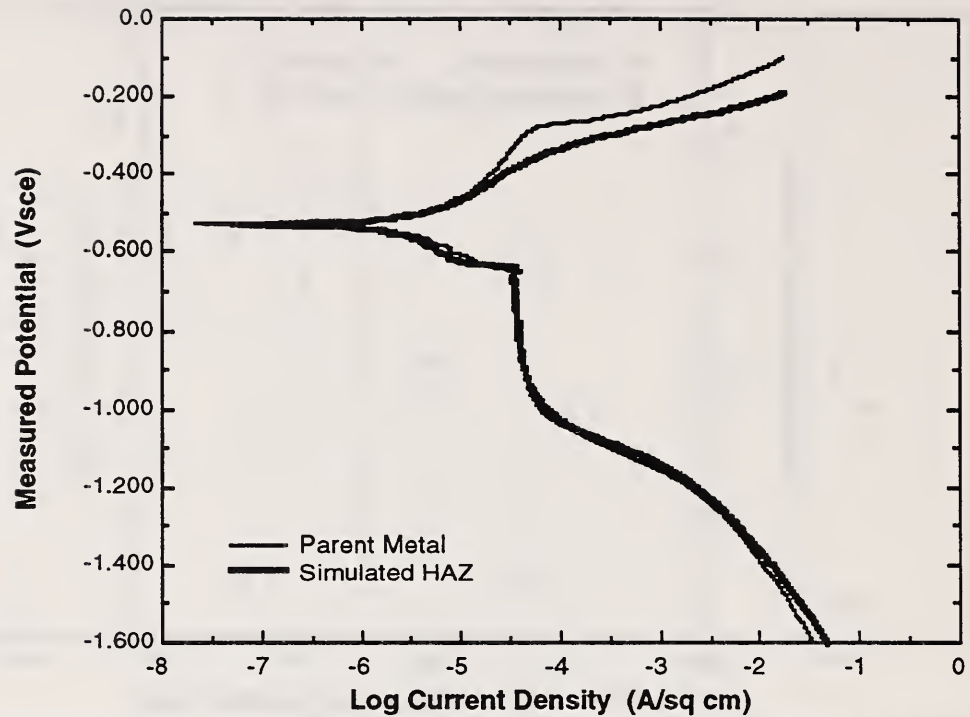


Figure 7a Potentiodynamic scan of the HY-100 parent metal and simulated heat affected zone in aerated ASTM artificial seawater at 1mv/sec scan rate.

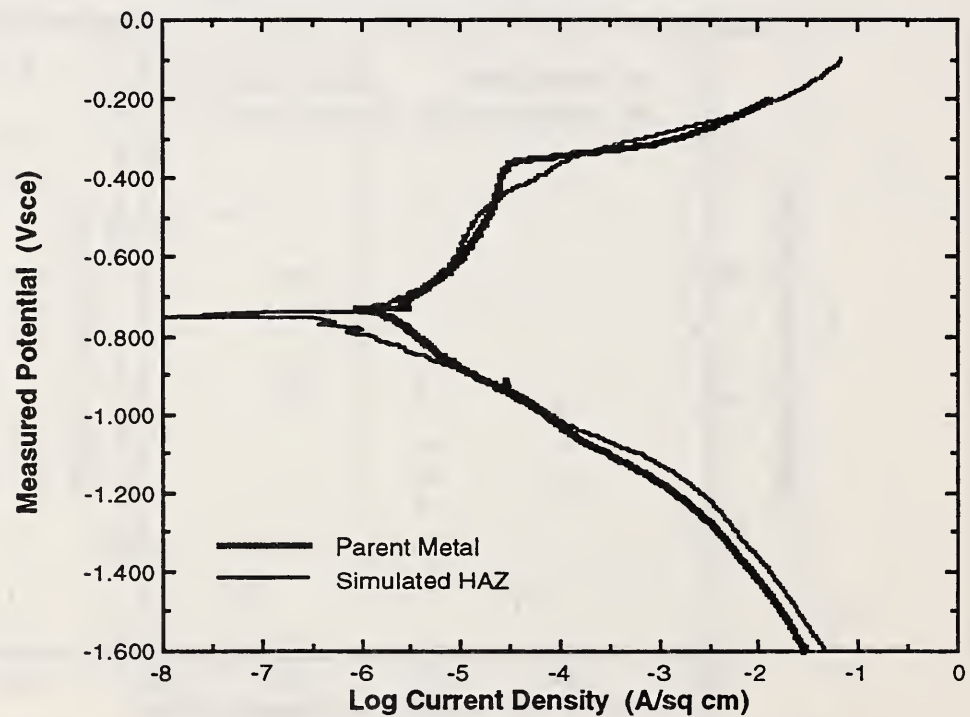


Figure 7b Potentiodynamic scan of the HY-100 parent metal and simulated heat affected zone in deaerated ASTM artificial seawater at 1mV/sec scan rate.

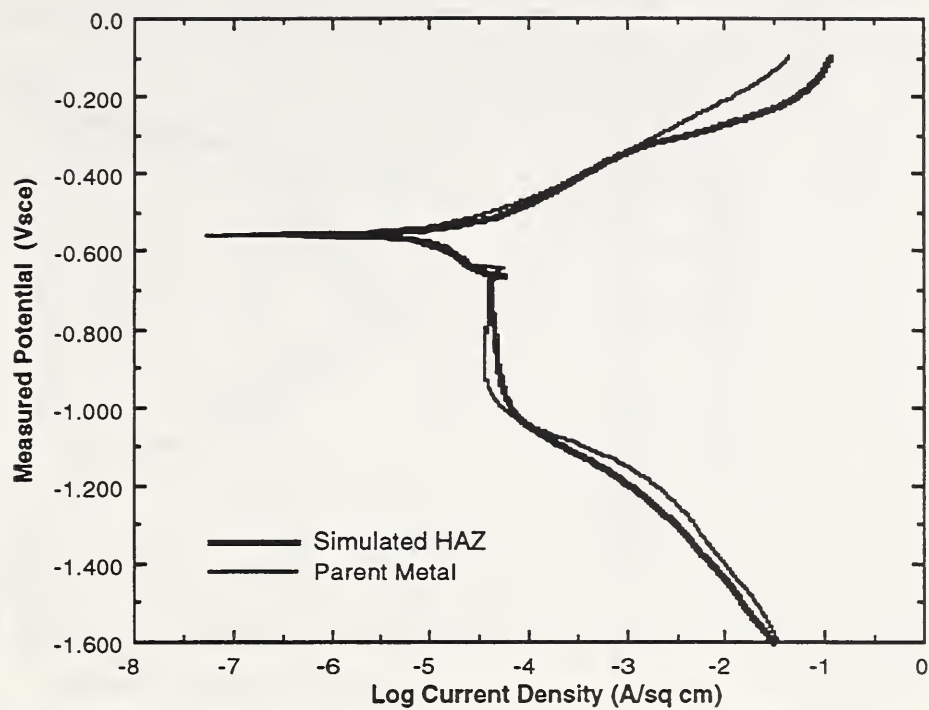


Figure 8a Potentiodynamic scan of the HSLA-100 parent metal and simulated heat affected zone in aerated ASTM artificial seawater at 1mV/sec scan rate.

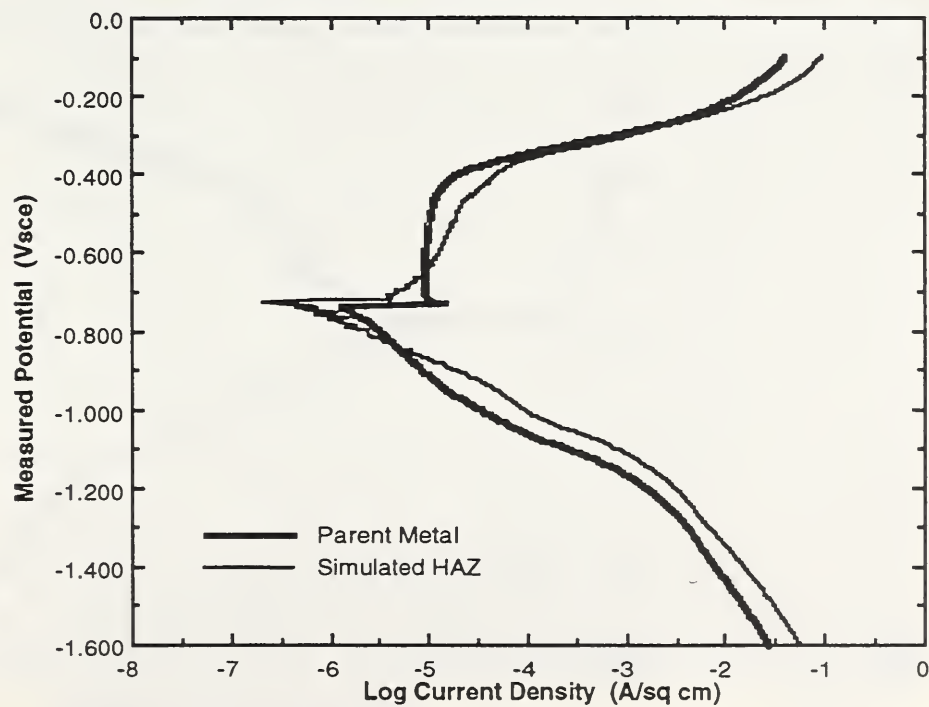


Figure 8b Potentiodynamic scan of the HSLA-100 parent metal and simulated heat affected zone in aerated ASTM artificial seawater at 1mV/sec scan rate.

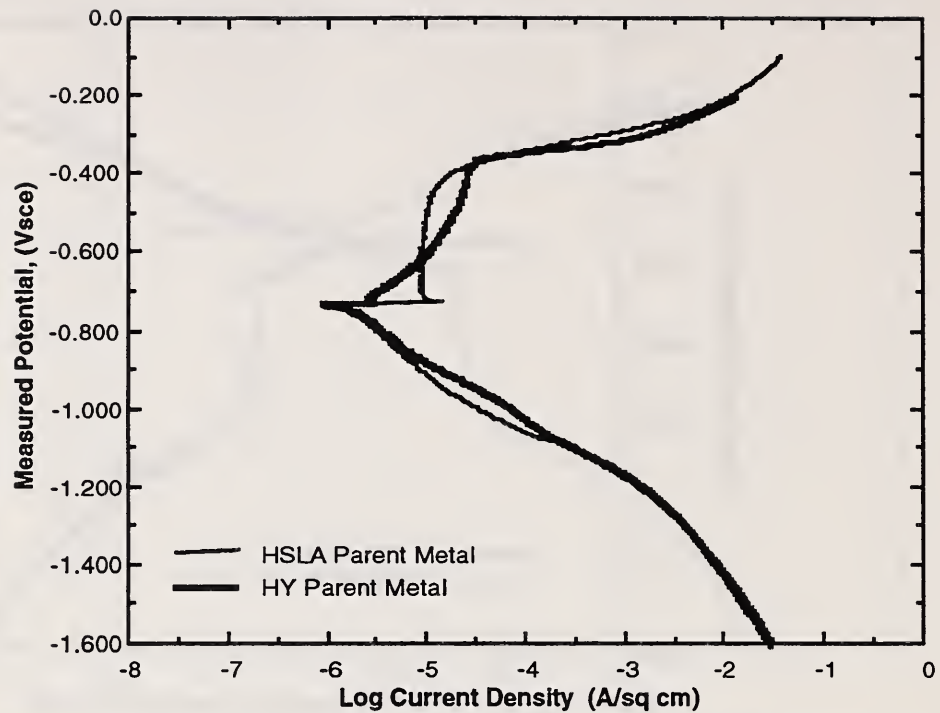


Figure 9a Comparison of the potentiodynamic scans for the HY-100 and the HSLA-100 parent metals in deaerated ASTM artificial seawater at 1mV/sec scan rate.

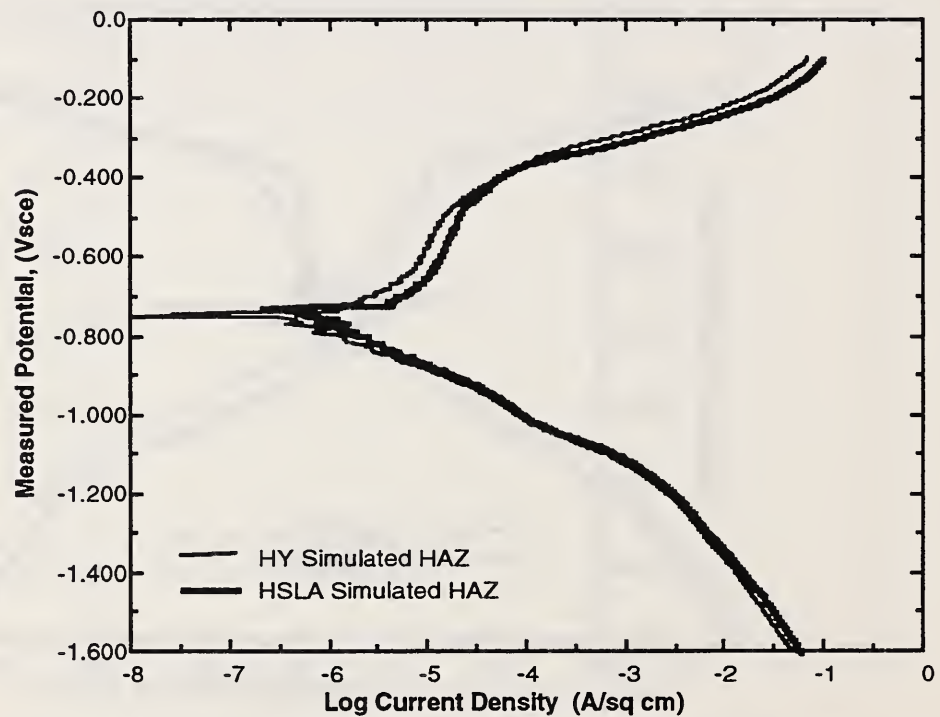


Figure 9b Comparison of the potentiodynamic scans for the HY-100 and the HSLA-100 simulated heat affected zones in deaerated ASTM artificial seawater at 1mV/sec scan rate.



Figure 10a

As polished view of the HY-100 parent metal showing the size and distribution of the observed inclusions.



Figure 10b

As polished view of the HSLA-100 parent metal showing the size and distribution of the observed inclusions.

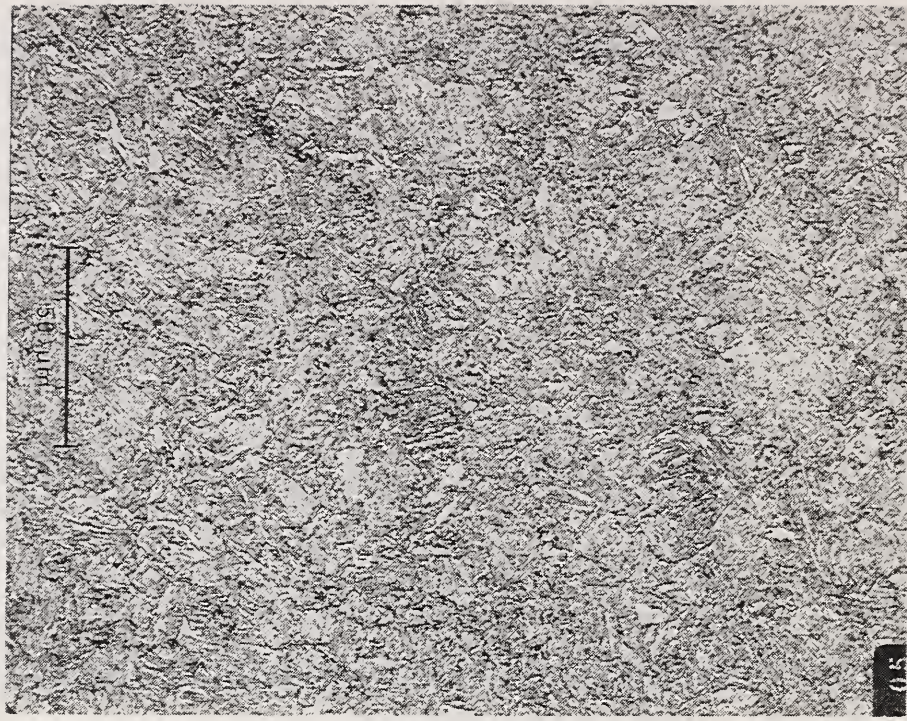


Figure 11a Optical micrograph of the HY-100 parent metal showing the quenched and tempered microstructure. (CLQ-1 etch)



Figure 11b Optical micrograph of the HSLA-100 parent metal showing the bainitic structure and niobium carbonitride precipitates. (CLQ-1 etch)



Figure 12a Optical micrograph of the HY-100 weld heat affected zone showing the greatest observed deviation from the parent metal microstructure. (CLQ-1 etch)

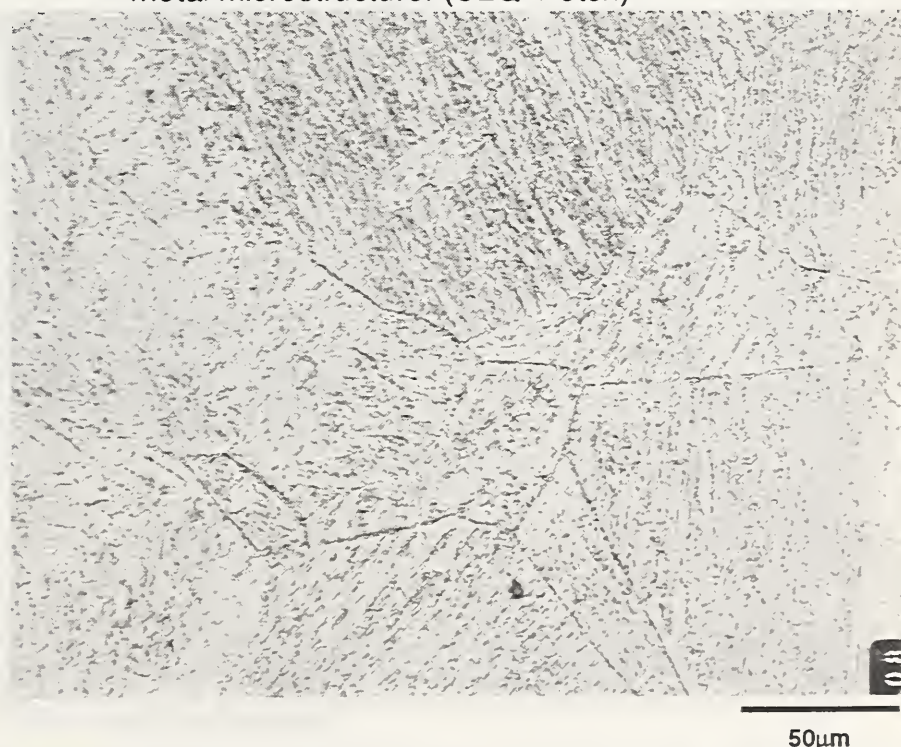


Figure 12b Optical micrograph of the HSLA-100 weld heat affected zone showing the greatest observed deviation from the parent metal microstructure. (CLQ-1 etch)

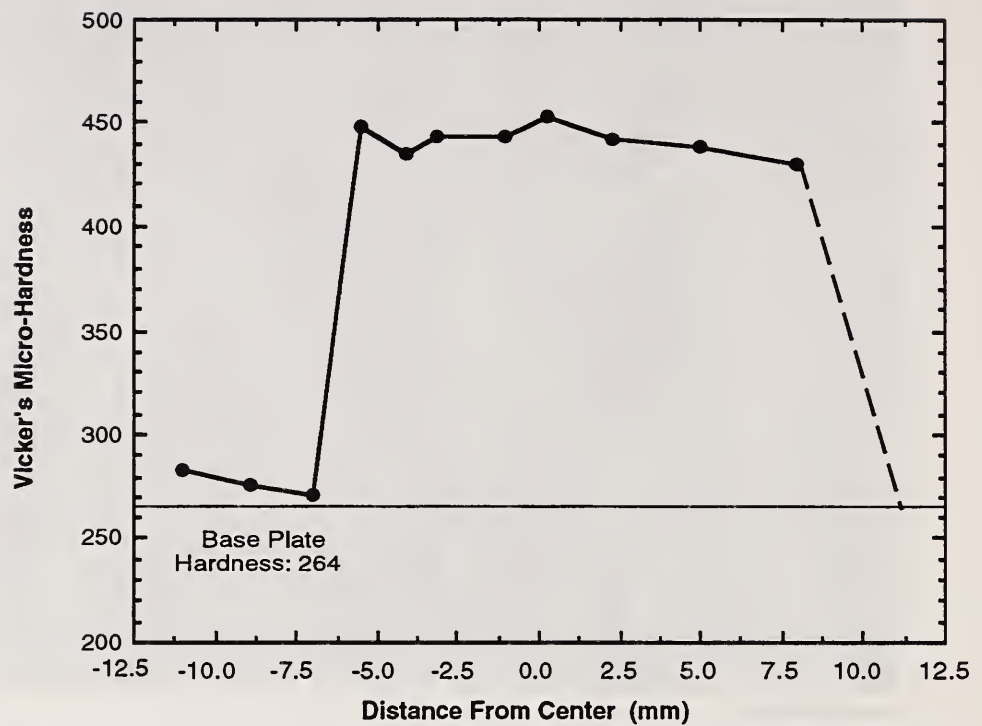


Figure 13a The variation in micro-hardness as measured from the center of the gauge section in a HY-100 simulated heat affected zone.

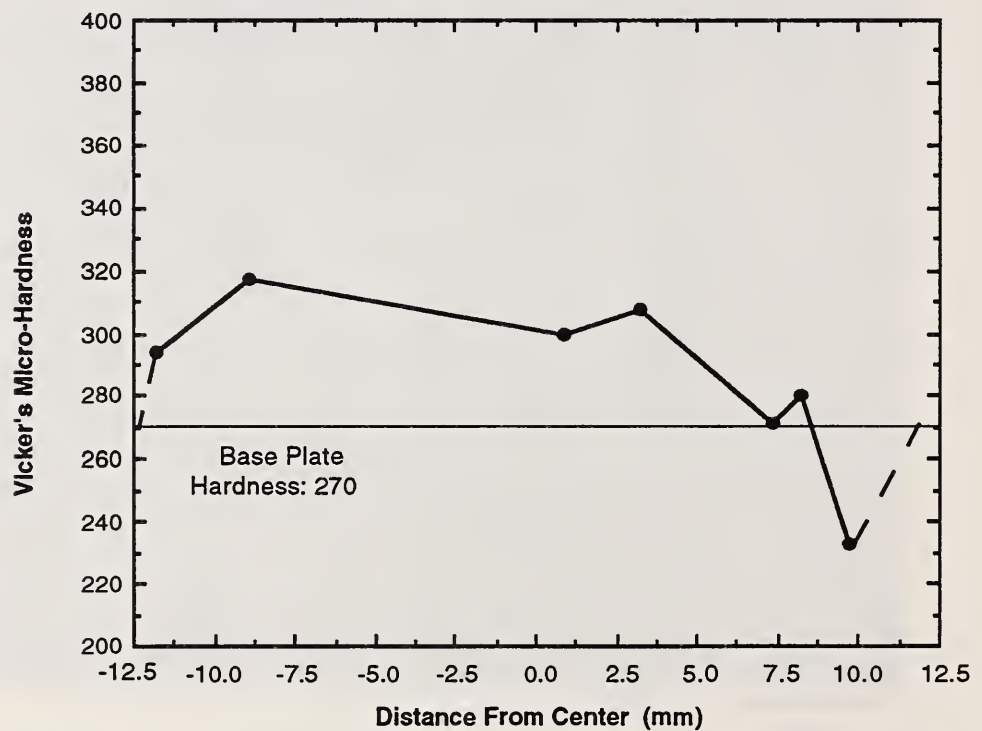


Figure 13b The variation in micro-hardness as measured from the center of the gauge section in a HSLA-100 simulated heat affected zone.



Figure 14a Low magnification scanning electron micrograph of the HY-100 heat affected zone showing the characteristic ductile behavior observed in the failures contained in Region I of Figure 6.

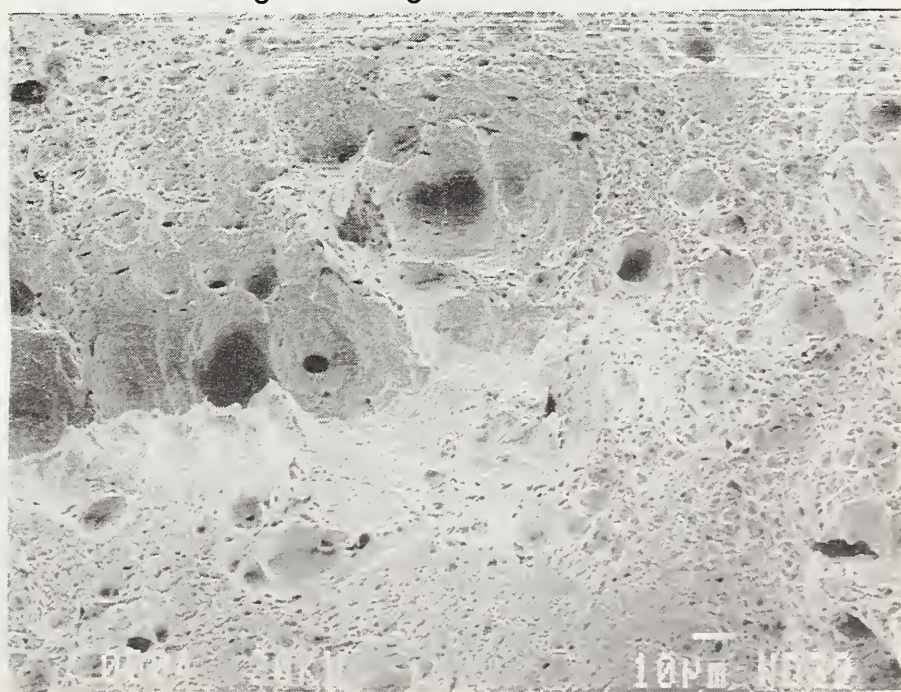
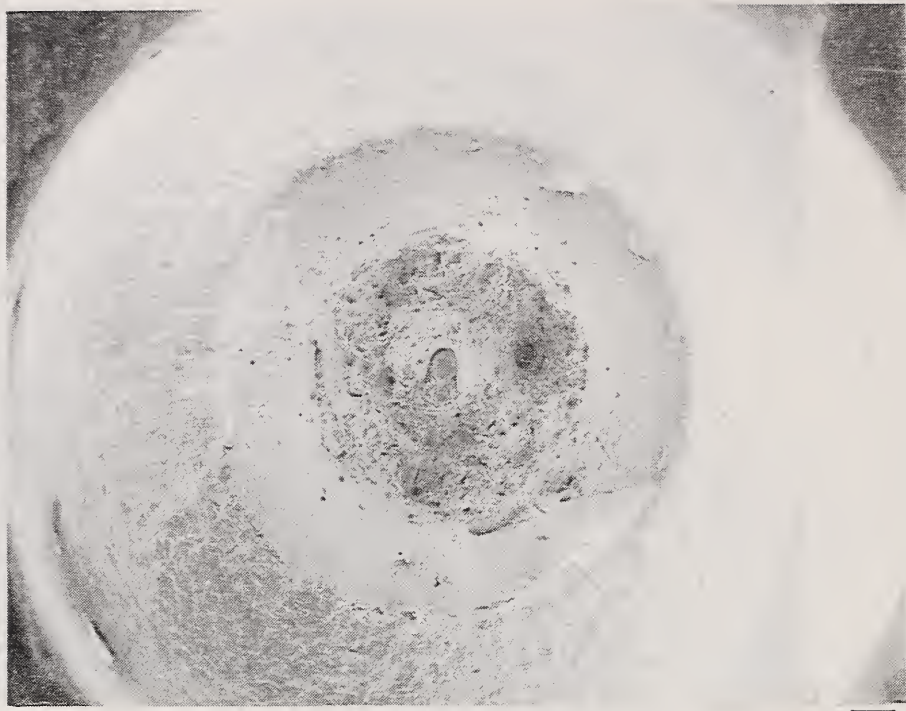
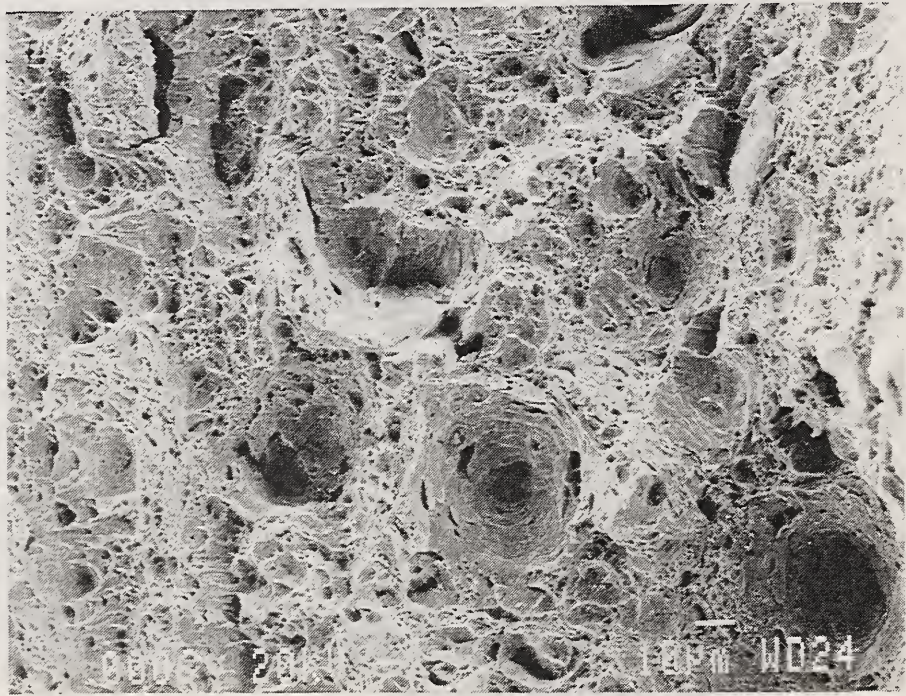


Figure 14b High magnification scanning electron micrograph from Figure 14a showing the general size and distribution of the observed microvoids.



100 μm

Figure 15a Low magnification scanning electron micrograph of the HSLA-100 heat affected zone showing the characteristic ductile behavior observed in the failures contained in Region I of Figure 6.



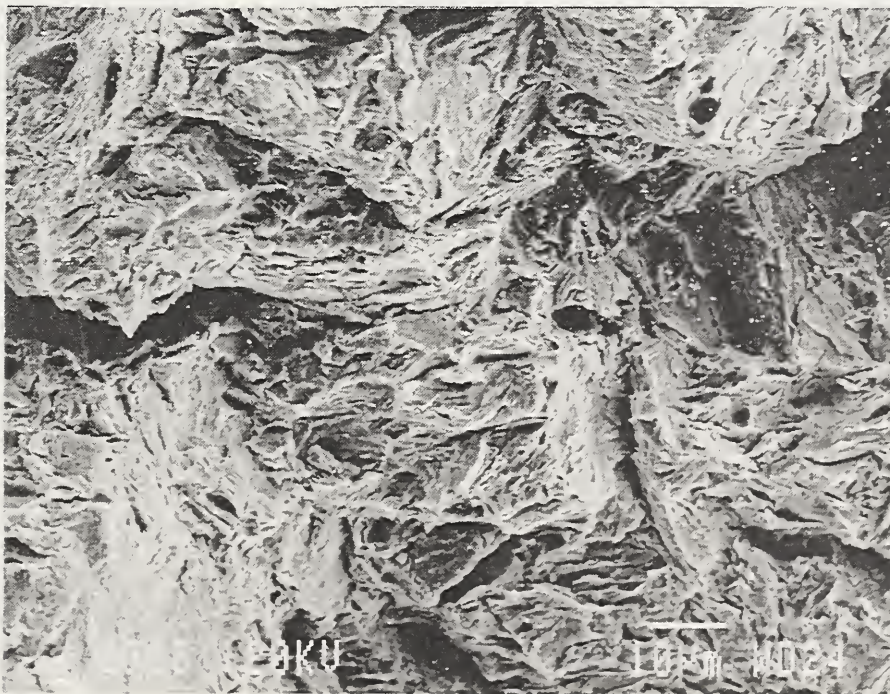
10 μm

Figure 15b High magnification scanning electron micrograph from Figure 15a showing the general size and distribution of the observed microvoids.



100 μm

Figure 16a Low magnification scanning electron micrograph of the HY-100 heat affected zone showing the embrittled behavior observed in failures contained in Region III of Figure 6.



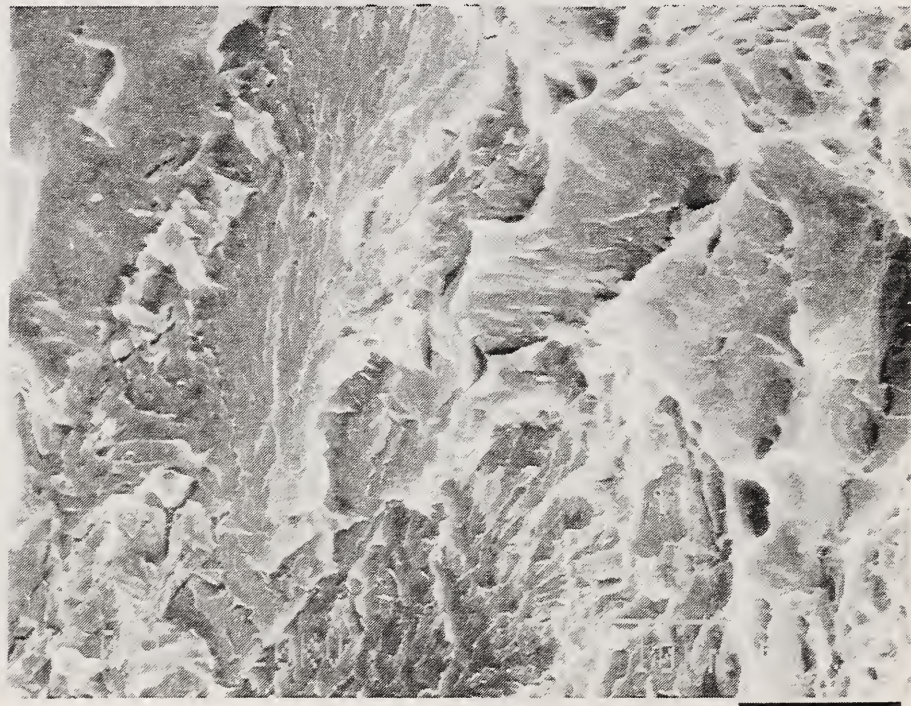
10 μm

Figure 16b High magnification scanning electron micrograph from Figure 16a showing the nature of the transgranular cleavage-like cracking observed.



100 μm

Figure 17a Low magnification scanning electron micrograph of the HSLA-100 heat affected zone showing the behavior observed in failures contained in Region III of Figure 6.



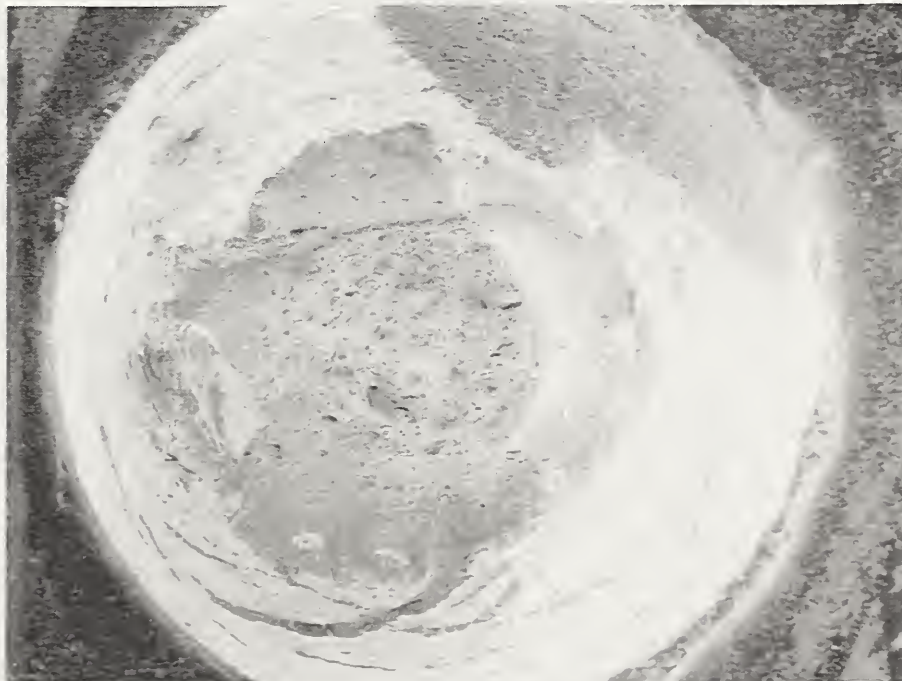
10 μm

Figure 17b High magnification scanning electron micrograph from Figure 17a showing the nature of the transgranular cleavage-like cracking observed.



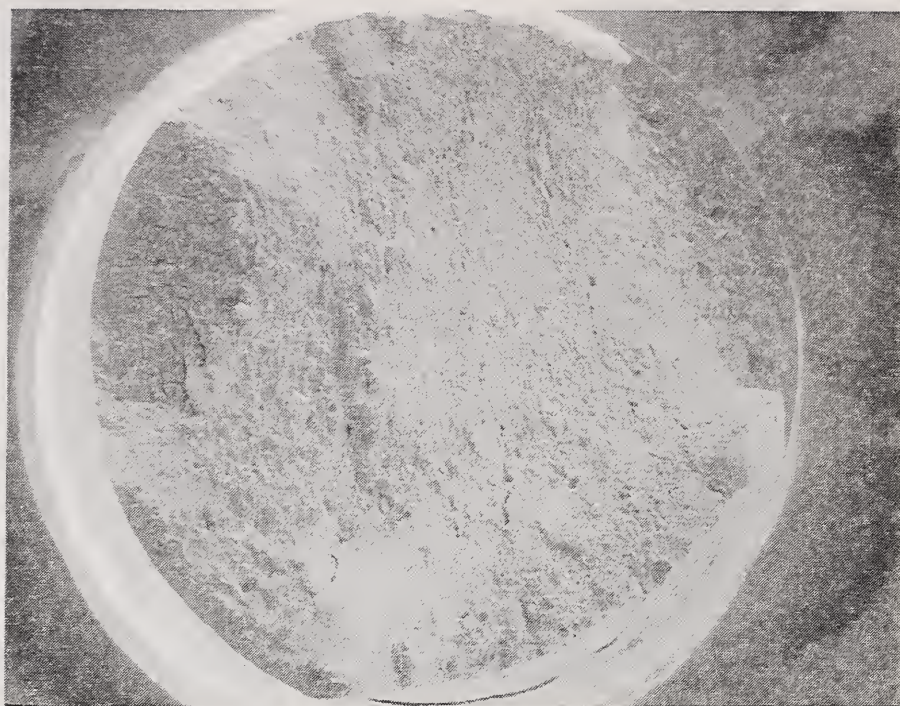
100 μm

Figure 18 Low magnification scanning electron micrograph of the HY-100 heat affected zone showing the mixed mode behavior observed in failures contained in Region II of Figure 6.



100 μm

Figure 19 Low magnification scanning electron micrograph of the HSLA-100 heat affected zone showing the mixed mode behavior observed in failures contained in Region II of Figure 6.



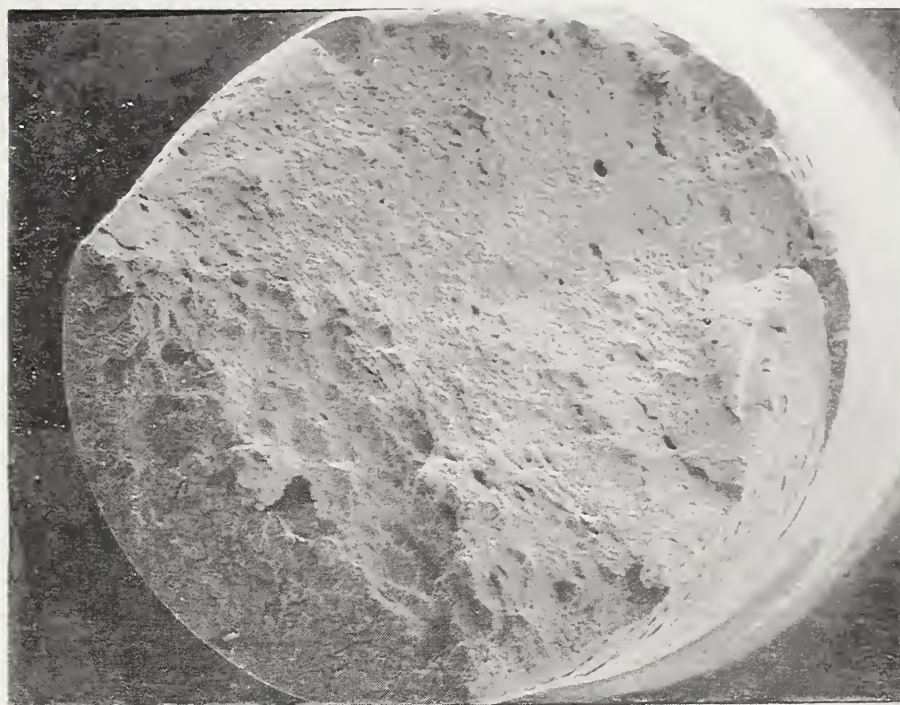
100 μm

Figure 20a Low magnification scanning electron micrograph of the HY-100 parent metal showing the embrittled behavior observed in failures contained in Region III of Figure 6.



10 μm

Figure 20b High magnification scanning electron micrograph from Figure 20a showing the nature of the transgranular cleavage-like cracking observed.



100 μm

Figure 21a Low magnification scanning electron micrograph of the HSLA-100 parent metal showing the behavior observed in failures contained in Region III of Figure 6.



10 μm

Figure 21b High magnification scanning electron micrograph from Figure 21a showing the nature of the transgranular cleavage-like cracking observed.

